



## Article

# The Key Role of Tin (Sn) in Microstructure and Mechanical Properties of Ti<sub>2</sub>SnC (M<sub>2</sub>AX) Thin Nanocrystalline Films and Powdered Polycrystalline Samples

Snejana Bakardjieva <sup>1,2,\*</sup>, Jiří Plocek <sup>1</sup>, Bauyrzhan Ismagulov <sup>1,3</sup> , Jaroslav Kupčík <sup>1</sup>, Jiří Vacík <sup>4</sup>, Giovanni Ceccio <sup>4</sup> , Vasily Lavrentiev <sup>4</sup> , Jiří Němeček <sup>5</sup> , Štefan Michna <sup>2</sup> and Robert Klie <sup>6</sup>

- <sup>1</sup> Institute of Inorganic Chemistry of the Czech Academy of Sciences, 250 68 Husinec-Rez, Czech Republic; plocek@iic.cas.cz (J.P.); ismagulov@iic.cas.cz (B.I.); kupcik@iic.cas.cz (J.K.)
- <sup>2</sup> Faculty of Mechanical Engineering, JE Purkyně University, Pasteurova 1, 400 96 Ústí nad Labem, Czech Republic; stefan.michna@ujep.cz
- <sup>3</sup> Department of Inorganic Chemistry, Faculty of Science, Charles University in Prague, Albertov 6, 128 43 Prague, Czech Republic
- <sup>4</sup> Nuclear Physics Institute, Czech Academy of Sciences, 250 68 Husinec-Rez, Czech Republic; vacik@ujf.cas.cz (J.V.); ceccio@ujf.cas.cz (G.C.); lavrentiev@ujf.cas.cz (V.L.)
- <sup>5</sup> Faculty of Civil Engineering, Czech Technical University in Prague, Thakurova 7, 166 29 Prague, Czech Republic; jiri.nemecek@fsv.cvut.cz
- <sup>6</sup> Department of Physics, The University of Illinois at Chicago, Chicago, IL 60607, USA; rfklie@uic.edu
- \* Correspondence: snejana@iic.cas.cz



**Citation:** Bakardjieva, S.; Plocek, J.; Ismagulov, B.; Kupčík, J.; Vacík, J.; Ceccio, G.; Lavrentiev, V.; Němeček, J.; Michna, Š.; Klie, R. The Key Role of Tin (Sn) in Microstructure and Mechanical Properties of Ti<sub>2</sub>SnC (M<sub>2</sub>AX) Thin Nanocrystalline Films and Powdered Polycrystalline Samples. *Nanomaterials* **2022**, *12*, 307. <https://doi.org/10.3390/nano12030307>

Academic Editors: Federico Cesano, Simas Rackauskas and Mohammed Jasim Uddin

Received: 16 December 2021

Accepted: 12 January 2022

Published: 18 January 2022

**Publisher's Note:** MDPI stays neutral with regard to jurisdictional claims in published maps and institutional affiliations.



**Copyright:** © 2022 by the authors. Licensee MDPI, Basel, Switzerland. This article is an open access article distributed under the terms and conditions of the Creative Commons Attribution (CC BY) license (<https://creativecommons.org/licenses/by/4.0/>).

**Abstract:** Layered ternary Ti<sub>2</sub>SnC carbides have attracted significant attention because of their advantage as a M<sub>2</sub>AX phase to bridge the gap between properties of metals and ceramics. In this study, Ti<sub>2</sub>SnC materials were synthesized by two different methods—an unconventional low-energy ion facility (LEIF) based on Ar<sup>+</sup> ion beam sputtering of the Ti, Sn, and C targets and sintering of a compressed mixture consisting of Ti, Sn, and C elemental powders up to 1250 °C. The Ti<sub>2</sub>SnC nanocrystalline thin films obtained by LEIF were irradiated by Ar<sup>+</sup> ions with an energy of 30 keV to the fluence of 1.1015 cm<sup>-2</sup> in order to examine their irradiation-induced resistivity. Quantitative structural analysis obtained by Cs-corrected high-angle annular dark-field scanning transmission electron microscopy (HAADF-STEM) confirmed transition from ternary Ti<sub>2</sub>SnC to binary Ti<sub>0.98</sub>C carbide due to irradiation-induced β-Sn surface segregation. The nanoindentation of Ti<sub>2</sub>SnC thin nanocrystalline films and Ti<sub>2</sub>SnC polycrystalline powders shows that irradiation did not affect significantly their mechanical properties when concerning their hardness (H) and Young's modulus (E). We highlighted the importance of the HAADF-STEM techniques to track atomic pathways clarifying the behavior of Sn atoms at the proximity of irradiation-induced nanoscale defects in Ti<sub>2</sub>SnC thin films.

**Keywords:** Ti<sub>2</sub>SnC; M<sub>2</sub>AX; powders; thin films; STEM; nanoindentation

## 1. Introduction

The MAX phases are a family of about 90+ carbides (or nitrides) synthesized up to now with a basic stoichiometry nomenclature M<sub>n+1</sub>AX<sub>n</sub>, where M is an early transition d metal (i.e., Sc, Ti, V, Cr, Zr, Nb, Mo, Hf, and Ta), A represents an element (mainly) from the IIIA or IVA groups of the periodic table (i.e., Al, Si, P, S, Ga, Ge, As, Cd, In, Sn, Tl, and Pb), and X is carbon or nitrogen. The index n can be 1, 2, or 3, so as the stoichiometry can vary, phases AMXMA (211), AMXMXMA (312), or AMXMXMXMA (413) can be formed [1]. The MAX phases have a hexagonal crystal structure (a space group D<sub>6h</sub><sup>4</sup>, P63/mmc) with two units per cell. The cell consists of the M<sub>6</sub>X octahedra that alternate with a single layer of the A elements [2].

The idea of the ternary transition metal carbides referred to as the H phases, where H denotes hexagonal close-packed structures, was developed by Nowotny and Jeitschko almost 60 years ago [3]. Later, the ternary transition metal carbides were classified as the M<sub>n+1</sub>

$AX_n$  phases [1–4] due to their unique hybrid structure with mixed covalent/ionic/metallic properties. This unusual conjunction influences their thermodynamic stability and mechanical properties and predicts that MAX phases could be highly regarded candidates for applications in extreme conditions. Some of the MAX compounds have already driven interest in nuclear engineering as materials with high potential for future fission and fusion reactors [5]. For instance, high radiation resistance was shown for the first time on titanium aluminum and titanium silicon carbides irradiated with high fluence heavy ions ( $Xe^+$ ,  $6.25 \times 10^{15}$  ions  $cm^{-2}$ ) [6]. The received experimental data suggested that after irradiation, the structure of the MAX compounds keeps well-ordered. This observation was acknowledged in new experiments [7] with other members of the MAX group. Titanium tin carbide (e.g.,  $Ti_2SnC$   $M_2AX$ ), discovered already in 1963 [3], demonstrates unusual material characteristics, such as high tolerance to mechanical damage, high modulus elasticity, and good integral stability at high temperature [8–11]. Surprisingly, there is a lack of relevant data on the ion beam and/or neutron radiation tolerance of  $Ti_2SnC$ . Perhaps this is due to the rather high cross sections for neutron-induced  $\gamma$ -(gamma) activation of the Sn isotopes ( $\sim 0.6$  b for natural Sn) with relatively long lifetimes (e.g.,  $\sim 129$  d for  $^{122}Sn + n$ ), which means that the  $Ti_2SnC$  may be unattractive for nuclear engineering technology. However, as a promising coating material,  $Ti_2SnC$  may still be interesting, and it is worth studying its irradiation resistance. The  $Ti_2SnC$  is especially synthesized using a finely dispersed powder of the Ti, Sn, and C phases, mixed in stoichiometric ratios, grounded, pressed, and sintered at high temperatures [12,13]. Other techniques, such as spark plasma sintering [14], have been invented and used for  $Ti_2SnC$  fabrication [15]. The applied methods, however, documented that together with the  $Ti_2SnC$  composite, some precipitates (such as  $TiC$ ,  $Ti_6Sn_6$ , or Sn) are also detected. It turns out that to fully transform the correct stoichiometric ratio of the Ti-Sn-C to the acceptable ternary  $M_2AX$  phase is still a challenge.

In this research, the  $Ti_2SnC$  thin nanocrystalline films (TNCFs) were synthesized using an unconventional low-energy ion facility (LEIF) based on ion beam sputtering combined with further a low-temperature thermal processing up to 150 °C. The  $Ti_2SnC$  powdered polycrystalline samples (PPS) were fabricated by simplified sintering of a compressed mixture consisting of (Ti, Sn, C) elemental powders. The goal of this study is to compare the morphological and nanomechanical features of  $Ti_2SnC$   $M_2AX$  materials prepared by using different synthetic methods. In addition, the irradiation tolerance of the  $Ti_2SnC$  TNCFs was examined. The irradiation was carried out by a heavy  $Ar^+$  ion with an energy of 30 keV to the fluence of  $1.10^{15}$   $cm^{-2}$ . We provide an experiment in the understanding of Sn atoms surface segregation and highlight the importance of aberration-corrected STEM techniques including high-angle annular dark-field detector (HAADF) to track atomic pathway clarifying the behavior of Sn atoms at the proximity of irradiation-induced nanoscale defects in  $Ti_2SnC$  TNCFs.

## 2. Materials and Methods

### 2.1. Synthesis of $Ti_2SnC$ $M_2AX$ PPSs

The  $Ti_2SnC$   $M_2AX$  PPSs were fabricated using a simplified method of sintering raw elemental powders. The experimental setup is presented in Figure 1a.

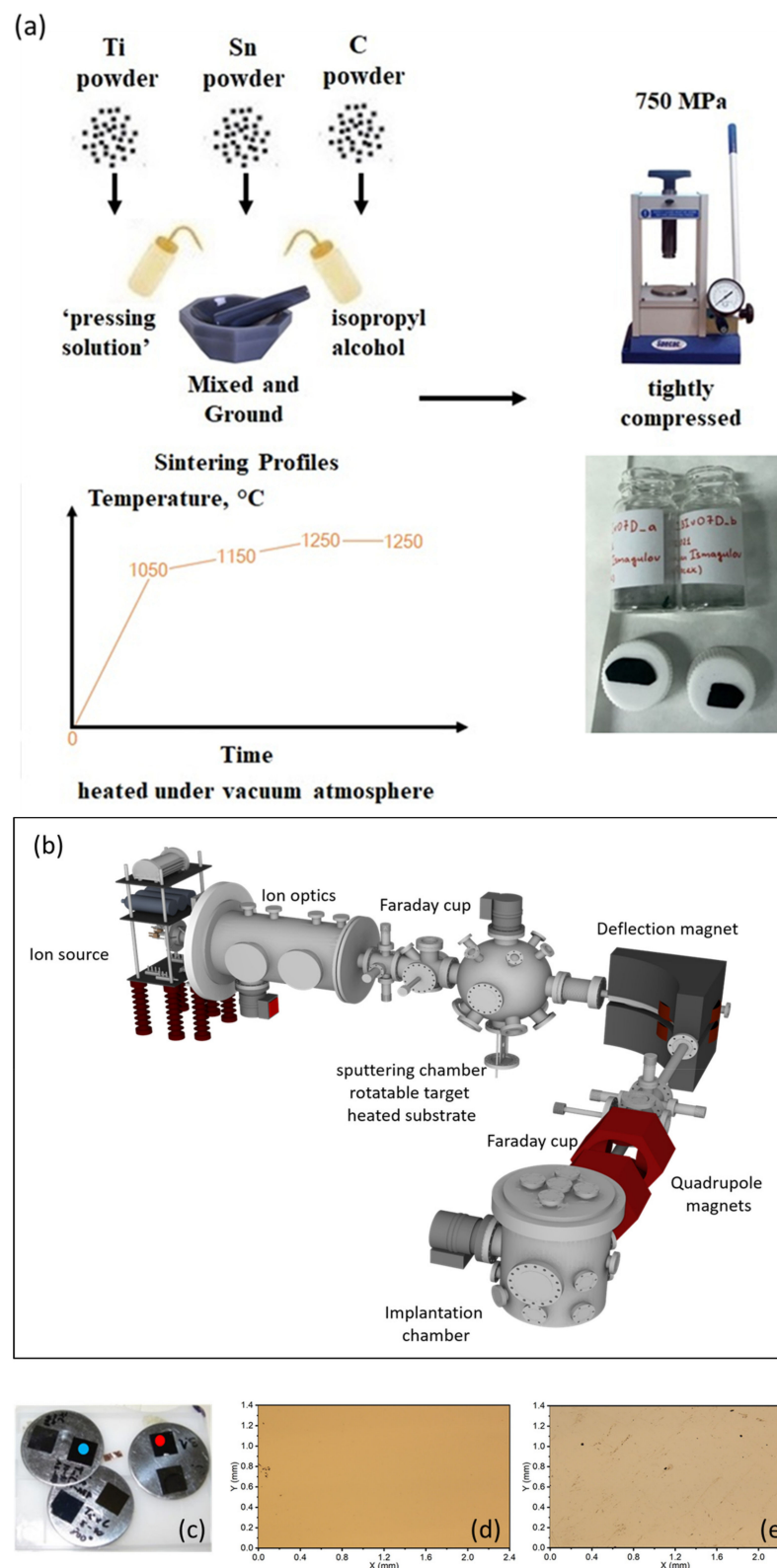


**Figure 1.** Schematic drawing of the  $\text{Ti}_2\text{SnC}$  synthesis (a)  $\text{Ti}_2\text{SnC}$  PPS by sintering of raw elemental powders with optical micrographs of  $\text{Ti}_2\text{SnC}$  PPS at low and high magnification. (b) Ion beam sputter deposition setup by LEIF for the synthesis of  $\text{Ti}_2\text{SnC}$  TNCFs. (c) Optical micrographs  $\text{Ti}_2\text{SnC}$  TNCFs by LEIF. (d) High magnification from the blue point marks the area where an optical micrograph of a single area for unirradiated  $\text{Ti}_2\text{SnC\_AGTNCFs}$  was acquired. (e) High magnification from the red point mark the area where an optical micrograph of a single area for irradiated  $\text{Ti}_2\text{SnC\_Ar}^+$  TNCFs was acquired.

Stoichiometric amounts of Ti (99.7%, Aldrich, powder), Sn ( $\geq 93\%$ , Aldrich, powder), and graphite (diamond powder) as raw materials were mixed with isopropyl alcohol at a 1/0.8/0.9 molar ratio and ground in an agate mortar. After thorough grinding, 0.1 mL of a ‘pressing solution’ (ethanol solution of polyethylene glycol 400, 1% *w/w*) was added to the fine ground suspension and mixed thoroughly again. After evaporation of the alcohol component, the solid mixture of reagents was tightly compressed (at a specified pressure of 750 MPa) to form a pellet with a diameter of 1.3 cm. The pellet was then placed into a corundum tube of a laboratory furnace and heated at a temperature up to 1250 °C under a vacuum. The optimal annealing regime to receive the Ti<sub>2</sub>SnC M<sub>2</sub>AX PPS was determined to be following (1. step 0–1050 C–20 C/min, 2. step 1050–1150C–10C/min, 3. step 1150–1250C–5C/min, 4. step 1250C–delay 2 h). The as-obtained pellet was milled and heated again under the same regime. The optical micrographs of Ti<sub>2</sub>SnC PPS are presented in Figure 1a.

## 2.2. Synthesis of Ti<sub>2</sub>SnC TNCFs

A set of Ti<sub>2</sub>SnC TNCFs was prepared by ion beam sputtering (IBS), as well as controlled thermal processing. The ions were generated in the high-current ion source (duoplasmatron) placed in the LEIF (lab-made Low Energy Ion Facility assembled by NPI) of the CANAM (Center of Accelerators and Nuclear Analytical Methods) research infrastructure in the NPI Rez [16]. The LEIF facility lets us utilize different gaseous ions with energy in the range of 100 eV to 35 keV, and an ion current up to 500  $\mu$ A. The beam spot size of the Gaussian-shaped ion beam was about 20 mm. In this report, the Ar<sup>+</sup> ions-beam has been used (apart from singly charged Ar<sup>+</sup>, double-charged Ar<sup>2+</sup> ions were also present, though only a fraction of a few %). The current and energy of the Ar<sup>+</sup> ion have been varied to measure the optimal values for the manufacture of the titanium tin carbide. For the fabrication of the Ti<sub>2</sub>SnC TNCFs, highly purified targets of Ti (99.995%), Sn (99.999%), and C (99.999%), all of the MaTeck (MaTeck Material Technologie & Kristalle GmbH, Juelich, Germany) materials have been used. The specimens were placed on a metallic (Cu) stocker (a frame with an equilateral triangle shape), each on a different side of the frame, that was mounted in the sputtering chamber of the LEIF system. The schema of the LEIF sputtering is presented in Figure 1b and described in detail elsewhere [17].

The targets with a size of about 5 cm in diameter covered the dimensions of the frame, so the sputtering from the target holder itself was stopped. The holder was connected to a metallic (Cu) axis (controlled from the outside of the chamber) and cooled down forcefully (by distilled water of an external cooling system) when specimens were overheated. The holder was revolving in 3 shifts with a speed of 1 rotation per 100 s. The revolution was performed automatically using a stepper motor (Accu-Glass Products. Inc., Valencia, CA, USA) operated by a PC. In each shift of 60°, a corresponding composite (Ti, Sn, or C) was sputtered for a definite period  $t_{\text{phase}}$  to deposit a necessary amount  $\Delta$  ( $\sim 10^{15}$  cm<sup>-2</sup>) of the specimens’ material on the substrate. The sputtering times were defined by the deposition rates  $DR_{\text{phase}}$  of the particular composites and by the stoichiometric ratio of the Ti<sub>2</sub>SnC phase (2:1:1):  $t_{\text{Ti}} = 2\Delta/DR_{\text{Ti}}$ ,  $t_{\text{Sn}} = \Delta/DR_{\text{Sn}}$ ,  $t_{\text{C}} = \Delta/DR_{\text{C}}$ . An approximately 1 nm thick layer with 2Ti+1Sn+1C atomic mixture was deposited during each rotation. The deposition was conducted on Si wafers or Mo TEM grids with ion energy of 25 keV and an ion current of 400 micro A. The deposition rates were held permanent and they were defined for Ti— $0.85 \times 10^{15}$  cm<sup>-2</sup>, Sn— $9.80 \times 10^{15}$  cm<sup>-2</sup> and C— $0.76 \times 10^{15}$  cm<sup>-2</sup> per min using RBS. A set of the samples was annealed at 150 °C for 24 h in a vacuum to induce interphase chemical interaction and complete formation of the stoichiometrically correct Ti<sub>2</sub>SnC M<sub>2</sub>AX phase. Samples were labeled Ti<sub>2</sub>SnC\_AGTNCF, where AG was denoted “as-growth” thin film. The Ti<sub>2</sub>SnC\_AGTNCF was further irradiated by 35 keV Ar<sup>+</sup> ions in order to examine their irradiation-induced resistivity. Optical micrographs Ti<sub>2</sub>SnC TNCFs obtained by LEIF are presented in Figure 1c–e.



### 2.3. Ion Beam Irradiation

In order to get pieces of knowledge about the radiation tolerance of the Ti<sub>2</sub>SnC\_AGNCFs, a heavy Ar<sup>+</sup> ion with an energy of 30 keV to the fluence of 1.10<sup>15</sup> cm<sup>-2</sup> was applied. It is assumed that Ar<sup>+</sup> ions with an energy of 30 keV generate an irradiated (damaged) area of 30 nm deep from the film surface. Using the SRIM-2013 code, the dpa value for this fluency was evaluated at 9.49 dpa (in the calculation, the density of Ti<sub>2</sub>SnC—6.36 g cm<sup>-3</sup>, displacement energy—25 keV, and ‘energy to recoil’—81 eVÅ<sup>-1</sup> were considered). The Ti<sub>2</sub>SnC\_AGNCFs were tested by several nuclear analytical methods. The thickness was examined with a sub-nanometer precision profilometer KLA-Tencor Alpha-Step IQ Surface Profiler/, as well as by Rutherford backscattering spectrometry (RBS; lab-made, assembled in NPI).

### 2.4. Methods of Characterization

The powder diffraction patterns of the Ti<sub>2</sub>SnC PPS were obtained with a PANalytical X’PertPRO MPD diffractometer (Malvern, United Kingdom) equipped with the Cu Kα tube (λ = 0.15406 nm). The diffractometer was operated at 40 kV and 30 mA with a 0.5° divergent slit coupled with a 0.1 mm receiving slit. Room temperature diffractograms were recorded in the transmission regime in the range from 5° to 85° at a 2θ step size of 0.01°. The phase composition of the measured powdered sample was calculated by the Rietveld analysis in an automatic mode of HighScore software 5.0 (Malvern, United Kingdom).

Scanning electron microscopy (SEM) was used for the characterization and imaging of the fine surface structure of the prepared Ti<sub>2</sub>SnC\_TNCFs and Ti<sub>2</sub>SnC PPS. For measurement, a JSM 6510LV system (low vacuum JEOL microscope, Jeol Ltd., Tokyo, Japan) with an acceleration voltage of 0.5–30 kV was used. For analysis, the secondary electron imaging mode (SE) was applied.

A detailed microstructural analysis of electron diffraction, and also elemental mapping, were carried out on a high-resolution transmission electron microscope (HRTEM) JEOL JEM 3010 Jeol Ltd., Tokyo, Japan). The microscope was operated at 300 kV (using a LaB<sub>6</sub> cathode; the point resolution was 1.7 Å), and it was equipped with an energy-dispersive X-ray (EDX) detector (Oxford Instruments, High Wycombe, UK) for elemental analysis, and a Gatan CCD camera (1024 × 1024 pixels) for image recording. The obtained images were analyzed using the Digital Micrograph software 3.5 package Gatan, California, USA), the EDX analysis was processed with the INCA software package (High Wycombe, UK). Electron diffraction patterns were evaluated using the ICDD PDF-2 database, Newtown Square, PA, USA [18] and ProcessDiffraction V\_8.7.1. Q software 7 package (Budapest, Hungary) [19]. For the TEM analysis, a small bit of the pellet sample was crushed, dispersed in ethanol, and the obtained suspension was sonicated for 2 min. A drop of the very dilute suspension was then placed on a holey-carbon coated Cu-grid and allowed to dry by evaporation at ambient temperature.

The atomic resolution Z-contrast images of Ti<sub>2</sub>SnC\_AGNCFs and Ti<sub>2</sub>SnC\_Ar<sup>+</sup>TNCFs were collected using the JEOL ARM200CF (Jeol Ltd., Tokyo, Japan) aberration-corrected STEM with a cold-field emission gun operated at an acceleration voltage of 80 kV. The high-angle annular dark-field (HAADF) images were acquired using an annular dark-field detector with a collection angle ranging from 90 to 175 mrad. The probe convergence semi-angle was set to 29 mrad, which yields a probe size of 1 Å at 80 kV and a probe current of 62 pA [20].

The surface topography of the Ti<sub>2</sub>SnC\_TNCFs fabricated by LEIF was studied by atomic force microscopy (AFM) using the NTEGRA scanning probe microscope (NT-MDT Spectrum Instruments, Moscow, Russia). The AFM experiments were performed under ambient conditions using tapping mode for the acquisition of the sample surface images (AFM topography).

The nanomechanical properties of the Ti<sub>2</sub>SnC\_AGNCFs, Ti<sub>2</sub>SnC\_Ar<sup>+</sup>TNCFs, and Ti<sub>2</sub>SnC PPS were inspected by nanoindentation with a Hysitron Tribolab TI-700 Nanoindenter (Bruker Nano GmbH, Berlin, Germany) equipped with a Berkovich tip. Indentations

were made at 4 distant locations (6 indentations at each), and each measurement consisted of 10 cycles with penetration depths between 20–150 nm (with a contact depth of 10–130 nm) to analyze changes induced by irradiation in the material's properties. The Hysitron TI-700 used with Berkovich tip is capable of quantitative measurements for depths larger than 10 nm, for which the tip calibration done on fused silica standard was performed. In the calibration procedure, the tip radius is not explicitly assessed, but the contact area is evaluated before the measurements. Measurements in larger depths can be considered accurate with the accuracy of the polynomial contact area calibration function ( $R^2 = 0.999$ ).

### 3. Results and Discussion

#### 3.1. Elemental Detection by Nuclear Analytical Methods

In Figure 2, both RBS and non-Rutherford spectra of  $Ti_2SnC\_AGTNCFs$  are presented together with the results obtained by simulations with SIMNRA code (performed on the Tandemtron 4230 MC). It was registered that  $Ti_2SnC\_ADTNCFs$  were contaminated by oxygen up to a level of about 35%. However, the ratio of the Ti, Sn, and C elements keeps up the stoichiometric ratio ( $Ti/Sn/C \sim 2/1/1$ ).

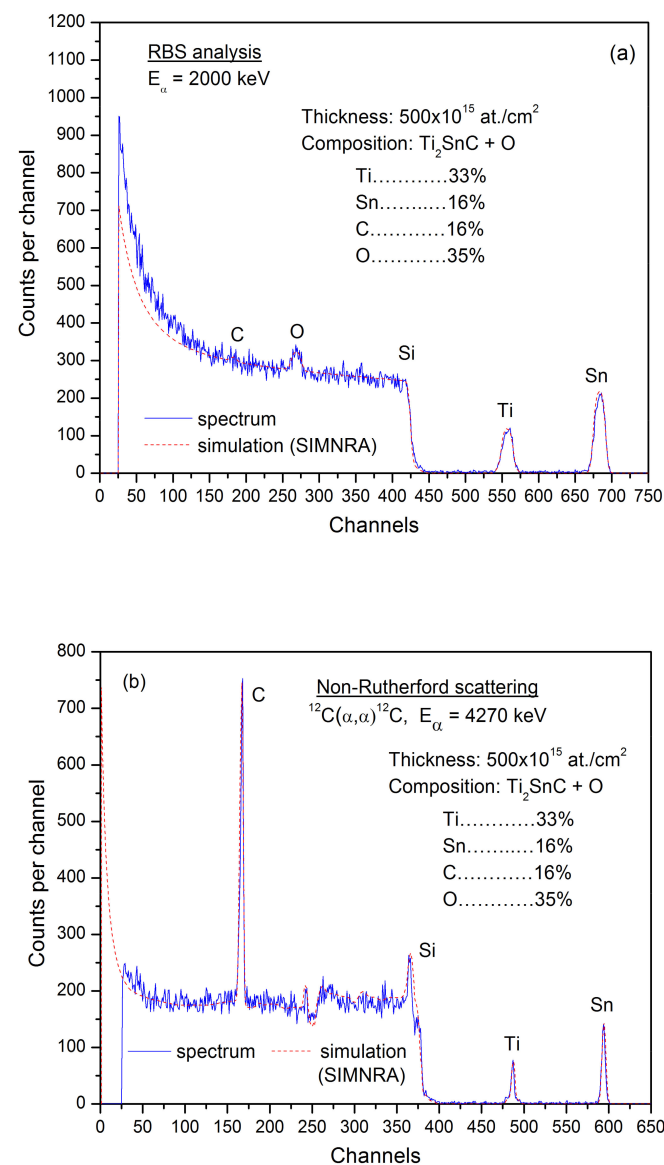


**Figure 2.** (a) RBS spectra of the  $Ti_2SnC\_AGTNCFs$ . (b) non-Rutherford scattering spectra of  $Ti_2SnC\_AGTNCFs$  by simulation of the energy spectra using the SIMNRA code.

We can suggest that  $\text{Ti}_2\text{SnC\_AGTNCFs}$  were (partially) oxidized either during the deposition process (with the residual oxygen in the sputtering chamber), or through the annealing in a relatively low-level vacuum of  $10^{-4}$  Pa [21]. Therefore, the synthetic challenge is to avoid oxidation contamination which occurs commonly when LEIF deposition is used [22].

The thickness of the  $\text{Ti}_2\text{SnC\_AGTNCFs}$  on the polished Si wafers with a size of about  $1 \text{ cm}^2$  was detected to be in the diapason  $460\text{--}920 \times 10^{15} \text{ cm}^{-2}$ .

### 3.2. Morphology of $\text{Ti}_2\text{SnC\_AD}$ , $\text{Ti}_2\text{SnC\_Ar}^+\text{TNCFs}$ , and $\text{Ti}_2\text{SnC\_PPS}$ Imaged by AFM and SEM

Figure 3 shows the AFM results obtained from analysis of the  $\text{Ti}_2\text{SnC\_AGTNCFs}$  and  $\text{Ti}_2\text{SnC\_Ar}^+\text{TNCFs}$  taken from the sample surface area of  $(1 \times 1) \mu\text{m}^2$ .

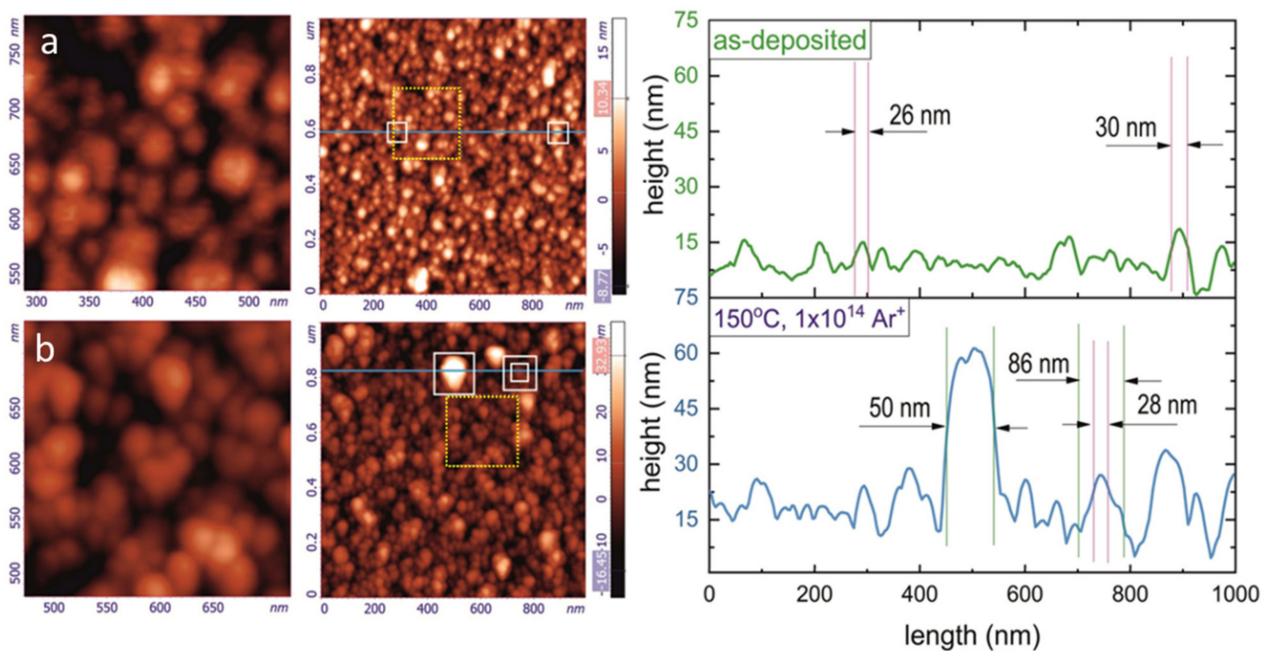


**Figure 3.** AFM characterization of the  $\text{Ti}_2\text{SnC\_AGTNCF}$  and  $\text{Ti}_2\text{SnC\_Ar}^+\text{TNCF}$ . (a) AFM topography of  $\text{Ti}_2\text{SnC\_AGTNCF}$  and image magnified part from the yellow dash square (right and left images, respectively) with its corresponding surface profile. (b) AFM topography of the surface profile of  $\text{Ti}_2\text{SnC\_Ar}^+\text{TNCF}$  and the image magnified part from the yellow dashed square (right and left images, respectively) with its corresponding surface profile.

Surface profile plots were prepared along the horizontal blue lines in the AFM images (see the plots from the right panel in Figure 3a,b). It is seen that the  $\text{Ti}_2\text{SnC\_AGTNCFs}$  surface (Figure 3a) consists of the nanoparticles (NPs), which are mostly separated each from other. Different color of the NPs reflects their different height, suggesting the formation of non-uniform agglomerates during the film deposition. The latter effect results in the relatively high surface roughness, which was found to be  $SR_{rms} = 3.275 \text{ nm}$  ( $SR_{rms}$  denotes the root mean square roughness of the surface). The details of the NPs agglomerations are seen in the magnified image of the  $(250 \times 250) \text{ nm}^2$ -sized surface area (see the AFM image from the left panel), selected by the dotted-line square in the original AFM image. Analysis of the magnified image and the surface profile reveals the size distribution of the NPs, with a lateral size of 20–30 nm. Annealing at  $150 \text{ }^\circ\text{C}$  ( $T_a = 150 \text{ }^\circ\text{C}$ ) and irradiation with the  $\text{Ar}^+$  ion beam modified the morphology of the  $\text{Ti}_2\text{SnC\_Ar}^+\text{TNCFs}$ . Surface roughness was found to be significantly higher ( $SR_{rms} = 7.057 \text{ nm}$ ) than that of  $\text{Ti}_2\text{SnC\_AGTNCF}$ . According to the magnified image (the left AFM image in Figure 3b) and the surface profile, bigger agglomerates with a lateral size of 50–90 nm appear on the  $\text{Ti}_2\text{SnC\_Ar}^+\text{TNCFs}$  surface. The spatial density of the agglomerations is also higher, and the size distribution shifting to the larger NP size was observed. It was rather hard to obtain AFM vital data

for  $\text{Ti}_2\text{SnC}$  PPS. The polishing technique and mechanical surface treatment during sample preparation were the main obstacles for representative AFM imaging. Despite that, Figure S1 shows the SEM surface morphology of the  $\text{Ti}_2\text{SnC}$  PPS. It is found that misaligned grains and pores are formed on the  $\text{Ti}_2\text{SnC}$  PPS surface during hydrothermal synthesis. A smooth surface and fully dense microstructure without defects can be seen in SEM micrographs of  $\text{Ti}_2\text{SnC\_AGTNCFs}$  (Figure S1a). When irradiation with an  $\text{Ar}^+$  ion beam was applied, the small round-shaped features on the surface of the  $\text{Ti}_2\text{SnC\_Ar}^+\text{TNCFs}$  appeared (Figure S1b), suggesting that  $\text{Ar}^+$  ion-beam irradiation-induced blistering and/or surface defects. In order for the structure of  $\text{Ti}_2\text{SnC\_AGTNCFs}$  and  $\text{Ti}_2\text{SnC\_Ar}^+\text{TNCFs}$  to be solved, atomic-resolution bright-field (BF) and HAADF imaging in Cs-corrected STEM was further performed and models for atomic ordering of  $\text{Ti}_2\text{SnC\_AGTNCFs}$  and  $\text{Ti}_2\text{SnC\_Ar}^+\text{TNCFs}$  structures were proposed.

### 3.3. Structural Analysis of the $\text{Ti}_2\text{SnC\_AGTNCF}$ with Atomic-Resolution STEM

Figure 4 shows the aberration-corrected BF and HAADF STEM micrographs of  $\text{Ti}_2\text{SnC\_AGTNCF}$  acquired from different magnification. Two regions can be distinguished in the HAADF-STEM images in Figure 4a,b; matrix with lower intensity (labeled 1) and well-crystallized spherical NPs (labeled 2), which present higher intensity (see a yellow boxed region in Figure 4b). This contrast can be associated with the atomic weight dependence of constituted elements. It should be noted that the contrast of Sn appears brighter than the Ti since the atomic number of Sn ( $Z = 50$ ) is larger than that of Ti ( $Z = 22$ ) in the HAADF electron scattering regime. The corresponding SAED (Figure 4c) confirms a mixture of two phases: tetragonal SnO (JCPDS 06-0395 space group  $P4/nmm$ ) and hexagonal  $\text{Ti}_2\text{InC}$  (JCPDS PDF 01-089-5590, space group  $P6_3/mmc$ ). A zoomed STEM image of the matrix is displayed in Figure 4f with an incident electron beam along the  $[001]$  direction. The measured lattice fringe spacings  $d_{(100)} = 0.27$  nm correspond to hexagonal  $\text{Ti}_2\text{SnC}$ . HAADF STEM analysis (Figure 4g-i) further provides additional evidence of the formation of SnO ( $\text{SnO-Sn}^{2+}$ ). In Figure 4i,  $(101)$  atomic planes with interplanar spacing  $d = 0.29$  nm for tetragonal SnO with growth in the  $c$  parameter direction on the surface of  $\text{Ti}_2\text{SnC}$  can be seen. Therefore, a protective  $\text{Ar}_2$  atmosphere could avoid the oxidation of Sn to the thermodynamically more stable  $\text{SnO}_2$  ( $\text{SnO}_2\text{-Sn}^{+4}$ ) [23,24]. A similar mechanism of SnO formation/ $\text{SnO}_2$  avoiding was reported upon using a protective  $\text{N}_2$  atmosphere for the synthesis of uniform nanocrystalline SnO layers [25,26].

Simultaneously performed EDS-STEM quantitative analysis (Figure S2a) confirmed the same elements (Ti, Sn, C, O) as detected by RBS and non-Rutherford scattering (see Figure 2). It can be seen from the elemental distribution maps (Figure S2b) that the mapping image of Sn is interconnected with the O mapping image. Such a correspondence reveals that Sn appears in oxygen-enriched regions, for example, spherical shaped NPs on the surface, and indicates that Sn can exist as an Sn-oxide rather than metal Sn [27].



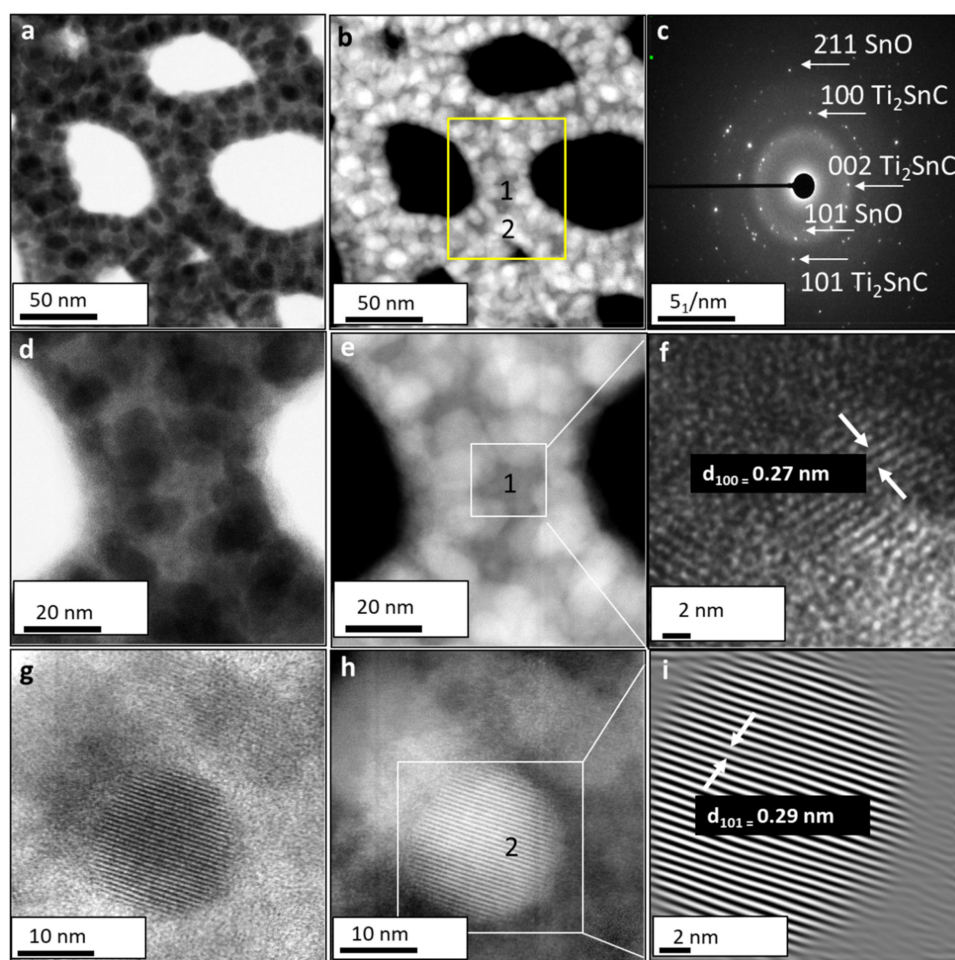


**Figure 4.** Aberration-corrected STEM images of unirradiated  $\text{Ti}_2\text{SnC\_AGTNCF}$ . (a) Low magnification BF-STEM image and (b) HAADF-STEM image where yellow boxed area outlines matrix with lower intensity (labeled 1) and brighter grains (labeled 2). (c) Corresponding SAED pattern showing atomic planes of SnO and  $\text{Ti}_2\text{SnC}$ . (d) High magnification BF-STEM image and (e) HAADF-STEM image showing zoomed matrix. (f) High magnification from the white marked area in (e) where lattice fringe spacing  $d_{(100)} = 0.27$  nm corresponds to hexagonal  $\text{Ti}_2\text{SnC}$  was indexed. (g) high magnification BF-STEM image and (h) HAADF-STEM image showing zoomed grain with higher intensity. (i) High magnification from the white marked area in (h) where lattice fringe spacing  $d_{(101)} = 0.29$  nm corresponds to tetragonal SnO was indexed.

### 3.4. Structural Analysis of the $\text{Ti}_2\text{SnC\_Ar}^+\text{TNCF}$ with Atomic-Resolution STEM

A structural anomaly in  $\text{Ti}_2\text{SnC\_Ar}^+\text{TNCF}$  was found to be driven during  $\text{Ar}^+$  ion beam irradiation. Low magnification BF (Figure 5a) and HAADF-STEM (Figure 5d) micrographs revealed well-crystallized nanograins. Figure 5b,e report magnified BF and HAADF STEM images, where interconnected disc-like NPs (labeled 1) and spherical NPs (labeled 2) were observed (Figure 4b,e).



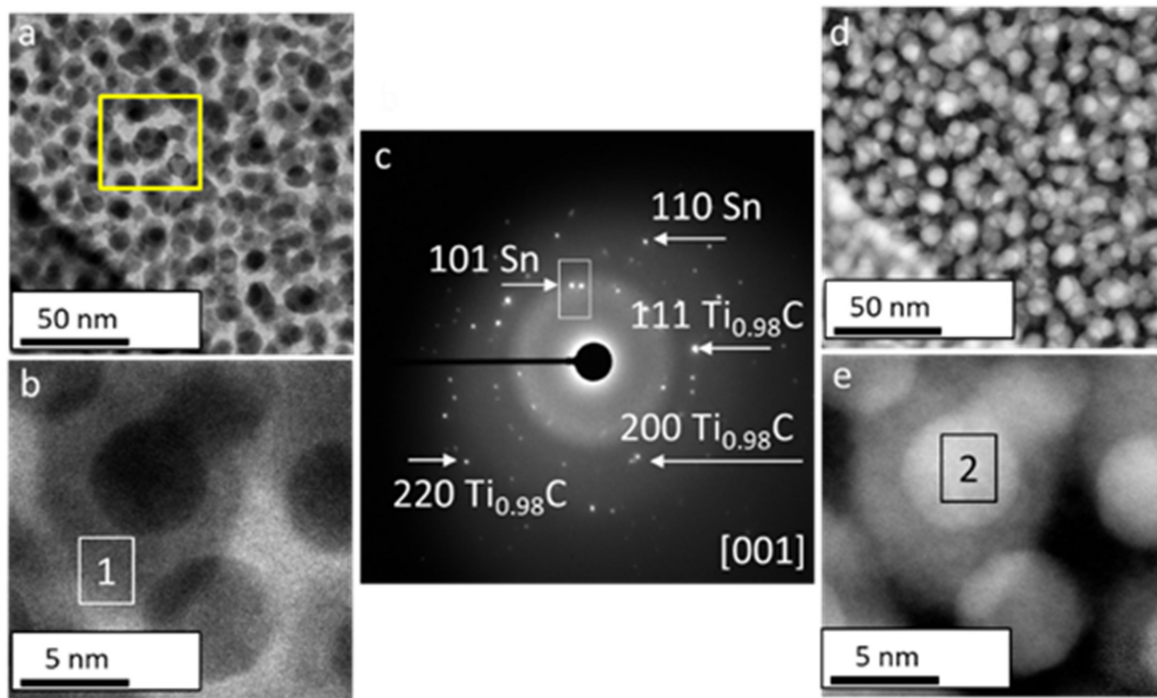


**Figure 5.** Aberration-corrected STEM images of irradiated  $\text{Ti}_2\text{SnC}_{\text{Ar}^+}\text{TNCF}$ . BF and HAADF-STEM images of  $\text{Ti}_2\text{SnC}_{\text{Ar}^+}\text{TNCF}$  (a) low magnification BF-STEM image and (b) BF-STEM high magnification of single Sn particle. (c) SAED from yellow boxed region in (a) showing atomic planes of metallic Sn and  $\text{Ti}_{0.98}\text{C}$ . (d) HAADF-STEM image at low magnification and (e) HAADF-STEM image at high magnification of Sn particle appeared with bright contrast because of the contribution of scattered electrons to the Sn image.

Besides the distinct morphology, the SAED pattern (Figure 5b) taken from the yellow boxed area in Figure 5a did not match those of  $\text{Ti}_2\text{SnC}$ . It was found that the lattice spacing and the angle of hexagonal  $\text{Ti}_2\text{SnC}$  lattice structure undergo a fundamental transformation. For identified [001] zone axis, the main (111), (220), and (200) lattice planes for cubic  $\text{Ti}_{0.98}\text{C}$  phase (i.e., space group  $Fm-3m$ , JCPDS PDF No. 04-004-2862) were detected. Furthermore, brighter reflections on the ED patterns were found to be extremely close to the (101) and (110) planes, matching well with an  $\beta$ -Sn with tetragonal symmetry (i.e., space group  $I4/mmm$ , JCPDS PDF No. 00-018-1380). We noticed that some diffraction spots (white boxed in SAED pattern) do become dimmers. High contrast variation in the HAADF STEM image (Figure 5e) suggests that the surface of disc-like NPs (labeled 1) is covered with smaller spherical NPs with bright contrast (labeled 2). Concerning the difference in atomic numbers of constituent elements and approached distinct Z-contrast, we could infer that  $\text{Ar}^+$  ion beam irradiation promoted the growth of fine spherical  $\beta$ -Sn NPs running along disc-like  $\text{Ti}_{0.98}\text{C}$  NPs [28–30]. The proposed dual heterostructure that evolved under the  $\text{Ar}^+$  ion-beam irradiation process was further confirmed by aberration-corrected HAADF-STEM imaging and simulation of experimental SAED patterns. We discuss first the structure of disc-like NPs in Figure 6a. The FFT in the [110] orientation (inset in Figure 6a) reports the major lattice planes (111), (220), and (200) for the cubic  $\text{Ti}_{0.98}\text{C}$  phase. Figure 6b shows an aberration-corrected HAADF-STEM image viewed along with the [001] zone axis. The structure is maintained to the surface on the (001) planes as obtained from the yellow marked area in Figure 6a. At this surface, there are only bright atomic columns, suggesting an atomic arrangement expected for the lattice with the space group  $Fm-3m$ , where the  $\text{Ti}^{2+}$  ions occupy the tetrahedral sites. The structure model of  $\text{Ti}_{0.98}\text{C}$  is superimposed on the HAADF-STEM image. For irradiated  $\text{Ti}_2\text{SnC}_{\text{Ar}^+}\text{TNCF}$  the atomic stacking transforms from ABABA/ $\text{TiCSnCTi}$  to ABBA// $\text{TiCCTi}$  (Figure 6c) [21]. We could expect that the atomic arrangements change to ABBA because all Sn atoms are segregated from the  $\text{Ti}_2\text{SnC}$

lattice and transition from  $M_2AX$  to  $M_{0.98}X$  structure has occurred. The simulated ED pattern of cubic  $Ti_{0.98}C$  agrees with the experimental FFT. Simulated [001] HRTEM image at a focus value  $f = -440 \text{ \AA}$  and a thickness  $t = 19 \text{ \AA}$  in Figure 6d is in line with the experimental contrast. The Ti columns can be seen in the simulated [110] HRTEM image that the Ti position appears as bright dots. The interlayer spacing of 0.24 nm is between the (111) cubic planes in the  $Ti_{0.98}C$  structure. The unit cell for the cubic  $Ti_{0.98}C$  arrangement is overlaid on the simulated STEM image.

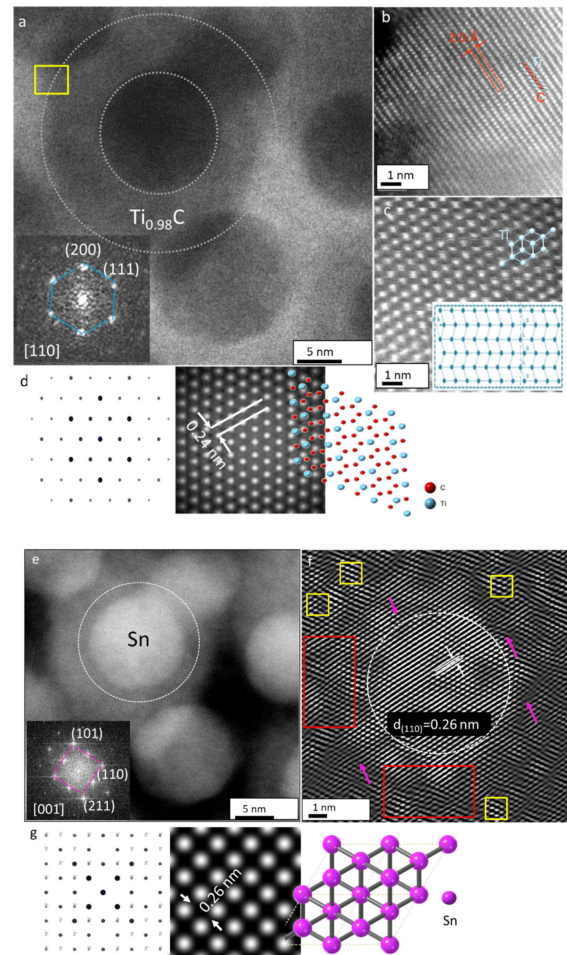


**Figure 6.** Crystalline structures of  $Ti_2SnC_{Ar^+}TNCF$ . (a) Aberration-corrected BF-STEM image with gray dashed lines outlines the disk-like grain as it degrades to  $Ti_{0.98}C$ . Inset: FFT phase diagrams of the corresponding STEM image. (b) HAADF-STEM image of the yellow boxed area in disk-like grain in (a) with clearly resolved atomic columns. The lattice spacing is measured as 2.0 Å. The structure model of  $Ti_{0.98}C$  is superimposed on the STEM image. (c) Atomic stacking transformation from ABABA in  $Ti_2SnC$  to ABBA in  $Ti_{0.98}C$ . (d) Simulated SAED patterns of  $Ti_2SnC_{Ar^+}TNCF$  structure. Transformation to the  $Ti_{0.98}C$  configuration with an interlayer spacing of 0.24 nm between the (111) planes due to the escape of Sn has occurred. The unit cell for  $Ti_{0.98}C$  composition with the cubic arrangement is overlaid on the simulated SAED image. Blue and red atoms refer to Ti and C, respectively. (e) aberration-corrected HAADF-STEM image with a white dashed line to outline the spherical NP as it segregates to  $\beta$ -Sn. Inset: FFT phase diagrams of the corresponding STEM image. (f) The corresponding HAADF-STEM image with clearly resolved atomic columns of tetragonal  $\beta$ -Sn. The lattice spacing is measured as 0.26 nm. (g) Simulated SAED patterns of the tetragonal  $\beta$ -Sn structure. Single Sn grain with an interlayer spacing of 0.26 nm between the (110) planes is observed. The unit cell for  $\beta$ -Sn composition with the tetragonal arrangement is overlaid on simulated SAED image: magenta atom refers to Sn.

The white contrast in the HAADF-STEM images in Figure 6e suggested that spherical NP with corresponding FFT (inset in Figure 6e) resemble tetragonal  $\beta$ -Sn. We can index the set of lattice planes (001), (101), and (200) and identify the [001] axis (the  $c$  axis) as the orientation of segregated Sn. The original STEM image was filtered by applying a Fourier mask to remove the noise and obtain clearer lattice periodicity (Figure 6f). As a result, lattice fringes with a  $d_{(110)}$  spacing of 0.26 nm, consistent with the tetragonal crystalline structure of Sn (JCPDS PDF No. 00-018-1380) was obtained. The weaker lattice fringes in the background appeared due to the adjacent cubic structure of the bottom disk-like  $\text{Ti}_{0.98}\text{C}$ . Here, we were able to identify the cubic  $\text{Ti}_{0.98}\text{C}$  (selected in yellow regions). Alongside the ordered structure, certain line defects—dislocation lines (marked with magenta-colored arrows) and collision cascades (selected in red regions) into the  $\text{Ti}_{0.98}\text{C}$  lattice were observed. These data appear to suggest that Sn segregation into small atomic clusters prefers to grow near the dislocation lines. It could be proposed that Sn clusters and irradiation-induced defect cores (dislocations and cascades) nucleated and grew together [31,32]. Simulated ED patterns of Sn along with the [110] zone axis (Figure 6g) show that  $d_{(110)} = 0.26$  nm crystal plane in tetragonal Sn is present. The atomic structure model of Sn along (010) in  $\text{Ti}_2\text{SnC\_Ar}^+\text{NCTF}$  is overlaid with a simulated ED pattern.

Figure S3a shows the EDS-STEM spectrum, atomic % of elements (Table inset in Figure S3a), and EDS elemental mapping (Figure S3b) of  $\text{Ti}_2\text{SnC\_Ar}^+\text{TNCF}$ . We found the presence of Ti, Sn, and C elements. The Ti/Sn atomic ratio in  $\text{Ti}_2\text{SnC\_Ar}^+\text{NCTF}$  decreases from the initial 1.17 in  $\text{Ti}_2\text{SnC\_AGNCTF}$  to the final 0.85 in  $\text{Ti}_2\text{SnC\_Ar}^+\text{TNCF}$ . It can be seen from the mapping images of Ti and C (Figure S3) that both elements become woven together and distributed all over the film, whereas the Sn mapping image suggests that Sn is not interconnected with Ti. Such an observation can indicate that Sn separated rather than being interwoven with  $\text{Ti}_2\text{SnC}$  structures, which was proved true from the HAADF-STEM and SAED observation. It is worthy to mention that the EDS spectra and the quantitative EDS mapping did not indicate the presence of oxygen. The absence of oxygen in  $\text{Ti}_2\text{SnC\_Ar}^+\text{NCTF}$  may be explained by the irradiation-induced ionization effect, which is reported to be pronounced not only in weakly bound Van der Waals elements but could be also occurred in systems with stronger bonds [33–35]. This ionization process can change both the equilibrium state and geometry of the overall system, including the  $\text{Ti}_2\text{SnC}$  matrix and surface SnO “etched out” the  $\text{Ti}_2\text{SnC}$ . Subsequently, the charge distribution in SnO, as well as its binding energy, may be altered. Therefore, we can assume that the 30 keV  $\text{Ar}^+$  with a fluence of  $10^{15} \text{ cm}^{-2}$  could provide enough energy to overcome the binding energy of 485.57 eV of the Sn  $3d_{5/2}$  core level of SnO, and further contribute to the fragmentation of the SnO [36]. These structural fragments could be Sn atoms and oxygen [37]. In the presence of  $\text{Ar}_2$ , chemical rearrangement of elements into  $\text{Ar}^+\text{-O}_2$  mixture and argon-oxygen ions as  $\text{Ar}(\text{O}_2)_n^+$ ,  $\text{Ar}_2(\text{O}_2)_m^+$  maybe generated [38]. Moreover, the presence of Ar peak in the EDS spectrum is very hard to evidence (Figure S3) since its only characteristic diffraction peak at 3.0 keV [39] is overlapped with Sn shoulder or probably because the Ar peak intensity is close to the noise level of the EDS spectrum. Additionally, the EDS technique could not be applicable for the detection of  $\text{Ar}_n(\text{O}_2)_m^+$  traces.

### 3.5. Mechanism of Irradiation-Induced Structural Transformation in $\text{Ti}_2\text{SnC}$ TNCFs

Although all of Sn containing ternary  $\text{Ti}_2\text{SnC}$   $M_2AX$  phase is very studied, the role of Sn element is still under debate. It is well known that Sn belongs to the Carbon family, group 14 (IVA) of the periodic table. Unlike other elements in the group, the Sn exists in two different allotropes, metallic  $\beta$ -Sn (malleable) and nonmetallic  $\alpha$ -Sn (brittle). Despite that  $\beta$ -Sn is the more common stable form, back transition process, from  $\alpha$ -Sn to  $\beta$ -Sn at low temperatures of  $-50$  °C is also well documented. This transition is called tin pest and hints at the different properties of Sn-based compounds. Apart from the recently reported ability of Sn to segregate in the early stages of crystallization and to act as heterogeneous



nucleation sites for the secondary precipitated phase [40], other competing mechanisms claimed out that the Sn atoms could be activated to excessive secondary segregation into facets along with the site of the yet crystallized matrix [41].

The segregation of  $\beta$ -Sn and formation of dual  $\beta$ -Sn/ $\text{Ti}_{0.98}\text{C}$  heterogeneous structure in irradiated  $\text{Ti}_2\text{SnC}_{\text{Ar}^+}\text{TNCf}$  was unraveled using atomic level direct experimental STEM observation (see Section 3.4). Close inspection of structures is present in the aberration-corrected HAADF images in Figure 7. The original ADF images are filtered using the annular mask tool in Digital Micrograph to remove high-frequency noise, and presented at the same magnification. Figure 7a reveals that  $\text{Ti}_2\text{SnC}_{\text{AGTNCf}}$  was dislocation-free, but lattice parameters obtained by Single Crystal software (Oxford, England) based on SEAD patterns were estimated to be larger than proposed for hexagonal  $\text{Ti}_2\text{SnC}$  (JCPDS PDF 01-089-5590, space group  $P6_3/mmc$ ). This observation suggests that residual strain in  $\text{Ti}_2\text{SnC}_{\text{AGTNCf}}$  has remained during the preparation.

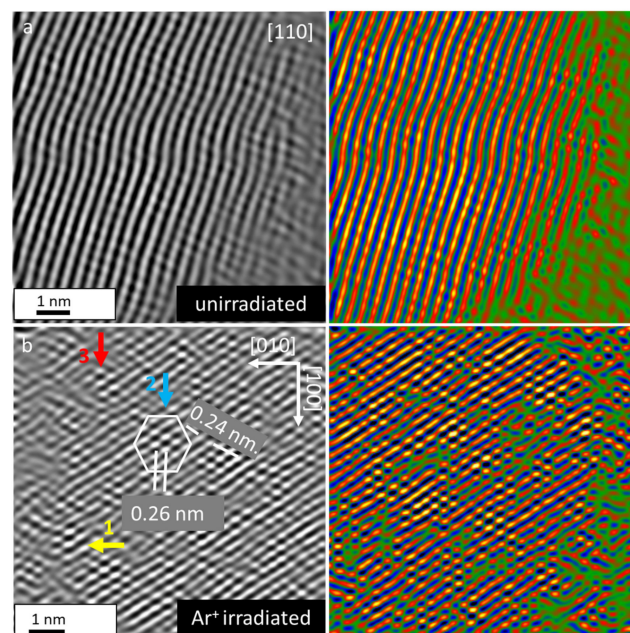


**Figure 7.** Aberration-corrected HAADF image of (a)  $\text{Ti}_2\text{SnC}_{\text{AGTNCf}}$  along the [110] direction and (b)  $\text{Ti}_2\text{SnC}_{\text{Ar}^+}\text{TNCf}$ . The regions of distorted structure are indicated by yellow, blue and red arrows. The atomic arrangements of  $\beta$ -Sn with spacing  $d_{(110)}$  of 0.26 nm interacted with  $\text{Ti}_{0.98}\text{C}$  with spacing  $d_{(111)}$  of 0.24 nm are well recognized. Corresponding filtered images to (a) and (b) by annular mask tool in Digital Micrograph are presented at the same magnification.

The  $\text{Ti}_2\text{SnC}_{\text{Ar}^+}\text{TNCf}$  (Figure 7b) was found to have a highly distorted structure. The regions of distorted structure are indicated with yellow, blue, and red arrows. Suffering from  $\text{Ar}^+$  ion beam irradiation, the Sn atomic displacement phenomenon, as the first consequence of irradiation, can result in the formation of point defects in  $\text{Ti}_2\text{SnC}$  lattice [42]. Additionally, irradiation-induced dislocations can provide channels for very fast Sn mass transport. Coming back to the thickness of the  $\text{Ti}_2\text{SnC}_{\text{AGTNCf}}$  estimated to be in the diapason  $460\text{--}920 \times 10^{15} \text{ cm}^{-2}$  (Section 3.1), an onset of the metamorphic layer due to melting of Sn ( $231.9^\circ\text{C}$ ) could take place during the  $\text{Ar}^+$  ion-beam irradiation. For  $\text{Ti}_2\text{SnC}$ , the migration energy barrier of Sn determined by ab initio calculation was found to be low enough (0.66 eV) to allow the self-diffusion of Sn atoms. These irradiation-induced defects can generate atomic transport in  $\text{Ti}_2\text{SnC}$  lattice and as a sequence, an extreme case, when all Sn atoms are extracted from  $\text{Ti}_2\text{SnC}$  could have occurred [43,44]. The STEM analysis reveals that in the region of the distorted structure indicated with a blue arrow, an isolated particle having a spacing of 0.26 nm that could be attributed to the  $\beta$ -Sn, is in contact with the particle, having space of 0.24 nm, that corresponded to  $\text{Ti}_{0.98}\text{C}$ . Even though staring

Ti<sub>2</sub>SnC\_AGTNCF has M<sub>2</sub>AX stoichiometric, Ar<sup>+</sup> ion-beam irradiation lowered stability of the Ti<sub>2</sub>SnC and promoted its decomposition into Sn and Ti<sub>0.98</sub>C. Our observations are in line with the attempts to correlate lattice parameters' c/a ratio with the stability of the 211 MAX phases as a function of Sn concentration. In addition, Ti<sub>2</sub>SnC combines a small M-atom with a large A-atom and the distortions due to the steric effect in both building blocks of MAX, octahedral and trigonal prisms, should be considered [45]. Therefore, radiation-induced dislocations and point defects in Ti<sub>2</sub>SnC can trigger diffusion and segregation of Sn atoms in irradiation-induced metastable Ti<sub>2</sub>SnC structure [46]. The rate at which the Sn concentration increases depends probably on the Ti<sub>2</sub>SnC NCs orientation, i.e., the precipitation of β-Sn has a specific crystallographic orientation relationship with the Ti<sub>2</sub>SnC matrix. In our case, β-Sn nucleated on Ti<sub>0.98</sub>C along the (110) planes as a result of the lattice stress, which induced a ⟨110⟩-oriented β-Sn pattern on the Ti<sub>0.98</sub>C surface (see Figure 7b) [47–49]. Concerning the above-discussed results, a model for describing the irradiation-induced behavior of Ti<sub>2</sub>SnC could be proposed to follow the steps: introducing of metastable Ti<sub>2</sub>SnC phase → spontaneously growth of Sn core at the initial stage of irradiation → interaction between Sn core and irradiation-induced defects → remove of metal β-Sn and restoring of Ti<sub>2</sub>SnC to equilibrium Ti<sub>0.98</sub>C concentration [21,50–52].

### 3.6. Structural Analysis of the Ti<sub>2</sub>SnC\_PPS with HRTEM/SAED

Microstructure and phase composition of Ti<sub>2</sub>SnC PPS were investigated by HRTEM/SAED and XRD. HRTEM micrograph in Figure 8a demonstrates another method of preparation graded material with various particle shapes. High magnification from the red boxed region in Figure 8a confirmed plates with an average size of 200 nm each, decorated with small nanograins located on the top edge of each plate (see Figure 8b). The corresponding SAED pattern (inset of Figure 8b) depicts the well-crystallized hexagonal Ti<sub>2</sub>SnC with resolved (100) and (101) lattice plane (JCPDS PDF 01-089-5590, space group P6<sub>3</sub>/mmc) along the [110] zone axis. An amorphous layer with a thickness of 10 nm (marked with red arrows in Figure 8b) was also well recognized. As expected, the HRTEM image (Figure 8b<sub>1</sub>) of single nanograin confirmed lattice fringes with spacing 0.23 nm observed for Ti<sub>2</sub>SnC. An HRTEM micrograph in Figure 8c corresponding to the blue framed area in Figure 8a revealed particles with different morphology as compared to the plate-shaped particles. Single NC with a length of about 50 nm and anisotropic 1D growth achieved through the preferred [111] orientation can be observed. The corresponding SAED pattern (inset in Figure 8c) confirmed the well-crystallized cubic TiC<sub>0.55</sub> with resolved (111) and (200) lattice plane and highly ordered lattice fringes with d<sub>(111)</sub> spacing of 0.24 nm (Figure 8c<sub>1</sub>) observed for TiC<sub>0.55</sub> with JCPDS PDF No. 04-018-5143.

Our HRTEM/SAED observations are in line with the XRD analysis of the Ti<sub>2</sub>SnC\_PPS. As one can see in Figure S4, the XRD pattern exhibits 70.4% of a single Ti<sub>2</sub>SnC phase following JCPDS PDF 04-005-0037. The diffraction peaks are sharp and confirmed a sample with high crystallinity. The dominance of the highest peaks, i.e., (103) for the in-plane pattern of hexagonal Ti<sub>2</sub>SnC phase, is well recognized. The calculated value for NPs size by Scherrer's formula was 120 nm [53]. In addition, there is a presence of 11.2% TiC<sub>0.55</sub> JCPDS PDF 04-018-5143 phase and 9% of Sn JCPDS PDF04-004-7745. Our XRD results are consistent with those of Li et al. [13] as well as with M.W. Barsoum, [54] which confirmed that the content of Ti<sub>2</sub>SnC increases with increasing the temperature. Therefore, when the reaction temperature increases up to 1250 °C, the Ti<sub>2</sub>SnC becomes the prevailing phase. Additionally, our results confirmed that when Sn presents in the composition range lower than 10%, no stable intermetallic impurities such as Ti<sub>3</sub>Sn, Ti<sub>6</sub>Sn<sub>5</sub>, Ti<sub>2</sub>Sn, and Ti<sub>5</sub>Sn<sub>3</sub> will be formed, and Ti<sub>2</sub>SnC can retain a single phase up to 70% homogeneity [55,56].



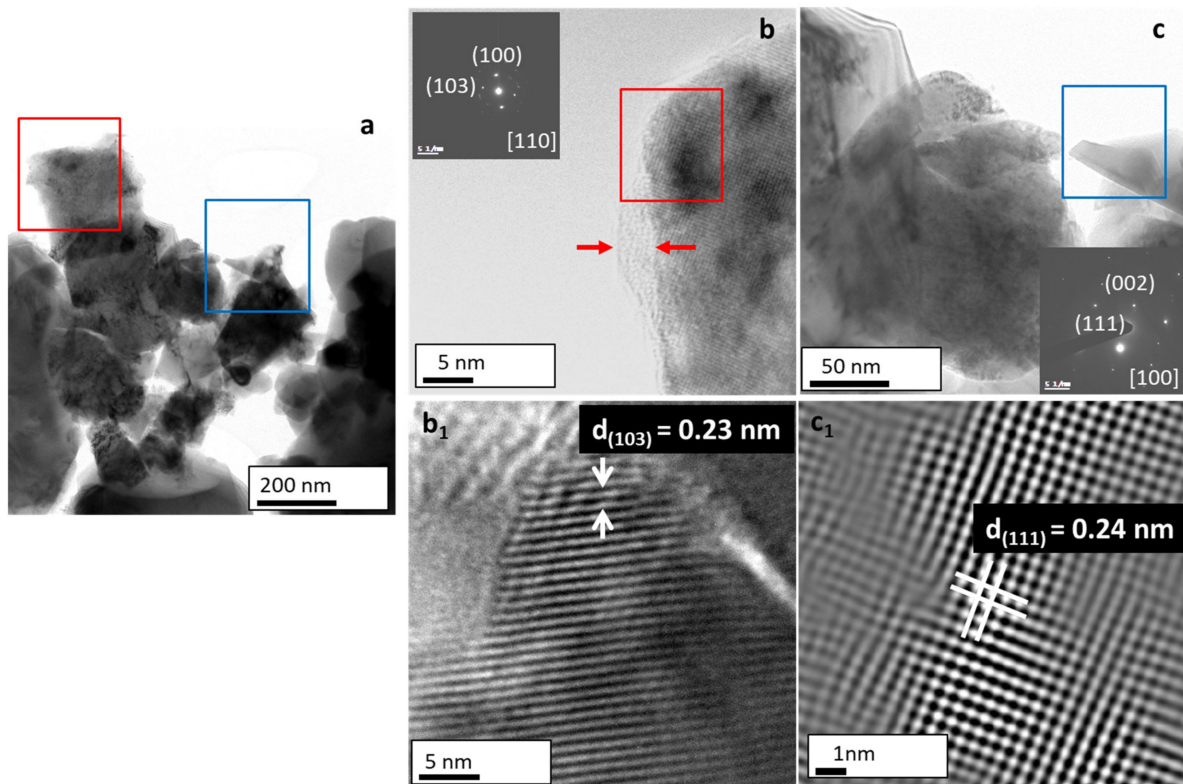


**Figure 8.** HRTEM study of  $\text{Ti}_2\text{SnC}$  PPS. (a) Representative low magnification micrograph of  $\text{Ti}_2\text{SnC}$ . (b) High magnification of red boxed region in (a) and SAED pattern with the (110) and (211) planes observed for cubic Sn. (c) High magnification of blue boxed region in (a) and SAED pattern with the (002) and (100) planes observed for hexagonal  $\text{Ti}_2\text{SnC}$ . (b<sub>1</sub>) The magnified HRTEM image of the selected grain in red boxed area in (b) with lattice spacing matching these indexed in SAED pattern and (c<sub>1</sub>) high magnification image of the selected grain in blue boxed area of  $\text{Ti}_2\text{SnC}$  in (c) with lattice spacing matching these indexed in SAED pattern.

### 3.7. Nanomechanical Properties $\text{Ti}_2\text{SnC}_{\text{AG}}$ , $\text{Ti}_2\text{SnC}_{\text{Ar}^+\text{TNCFs}}$ and $\text{Ti}_2\text{SnC}_{\text{PPS}}$

In this section, we consider the mechanical properties of  $\text{Ti}_2\text{SnC}_{\text{AGTNCF}}$ ,  $\text{Ti}_2\text{SnC}_{\text{Ar}^+\text{TNCF}}$ , and  $\text{Ti}_2\text{SnC}_{\text{PPS}}$ . Table 1 shows values of Young's modulus ( $E$ ) and hardness ( $H$ ) calculated from contact depths of 10–40 nm using linear extrapolation to zero depth (from 10–80 nm for  $\text{Ti}_2\text{SnC}_{\text{PPS}}$  samples, respectively). The reduced modulus ( $E_r$ ) and hardness ( $H$ ) were evaluated for each loading step by the Oliver and Pharr method [57]. Young's modulus ( $E$ ) was calculated from the reduced modulus based on the assumption of the sample Poisson's ratio of 0.24 [58]. Figures 9 and 10 show results of elastic moduli and hardness in individual points represented by dots in the figures while red lines in Figures 9 and 10 represent a linear fit from the 10–40 nm or 10–80 nm region on respective samples. The non-constant trend indicates an influence of the harder substrate for larger penetration depths meaning the true surface properties in the sub-10 nm region can be even lower. Extrapolated values to zero depth are theoretical surface characteristics not influenced by the substrate effects on  $\text{Ti}_2\text{SnC}_{\text{AG}}/\text{Ar}^+\text{TNCF}$  samples or structural effects in the case of the bulk samples  $\text{Ti}_2\text{SnC}_{\text{PPS}}$  pristine (non-irradiated) (Figure 11) and  $\text{Ti}_2\text{SnC}_{\text{PPS}}$  irradiated (Figure 12). Nevertheless, any comparison of pristine and irradiated samples made from the results holds. The values of the substrate Si/(001) wafer as reference material are also included [17].

**Table 1.** Young's modulus (E) and hardness (H) (values of linear fit at zero depth) of Ti<sub>2</sub>SnC\_AGTNCF (film), Ti<sub>2</sub>SnC\_Ar<sup>+</sup>TNCF (film), Ti<sub>2</sub>SnC\_PPS pristine (bulk), Ti<sub>2</sub>SnC\_PPS irradiated (bulk), and Si substrate.

Sample	E(GPa)	H(GPa)
Ti <sub>2</sub> SnC_AGTNCF (film)	87.7	2.48
Ti <sub>2</sub> SnC_Ar <sup>+</sup> TNCF (film)	97.6	2.44
Ti <sub>2</sub> SnC_PPS pristine (bulk)	104.9	2.56
Ti <sub>2</sub> SnC_PPS irradiated (bulk)	100.8	2.08
Si substrate, ref. [17]	166.6	15.3

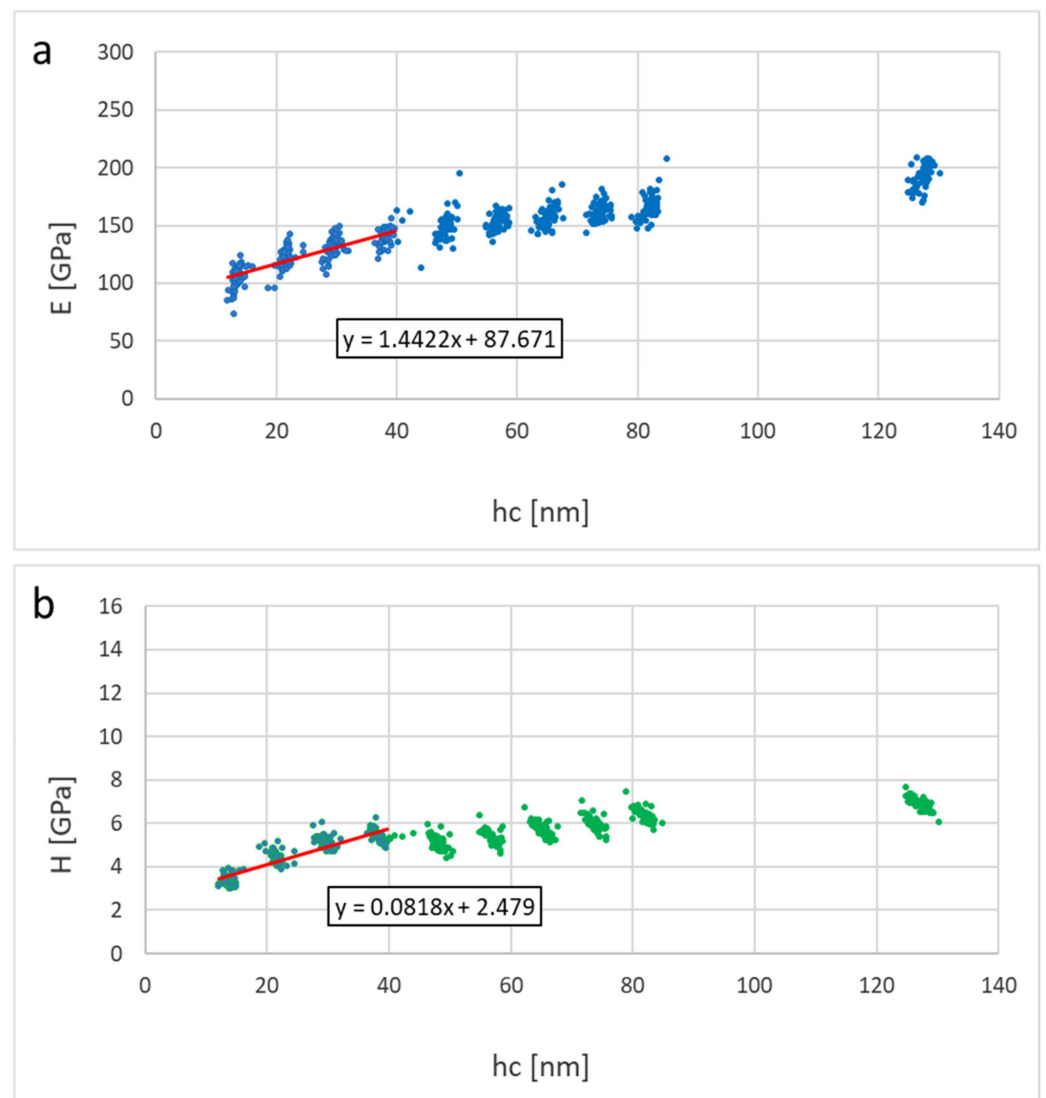


**Figure 9.** Results for Ti<sub>2</sub>SnC\_AGTNCF (a) Young's modulus vs. contact depth, (b) hardness vs. contact depth.

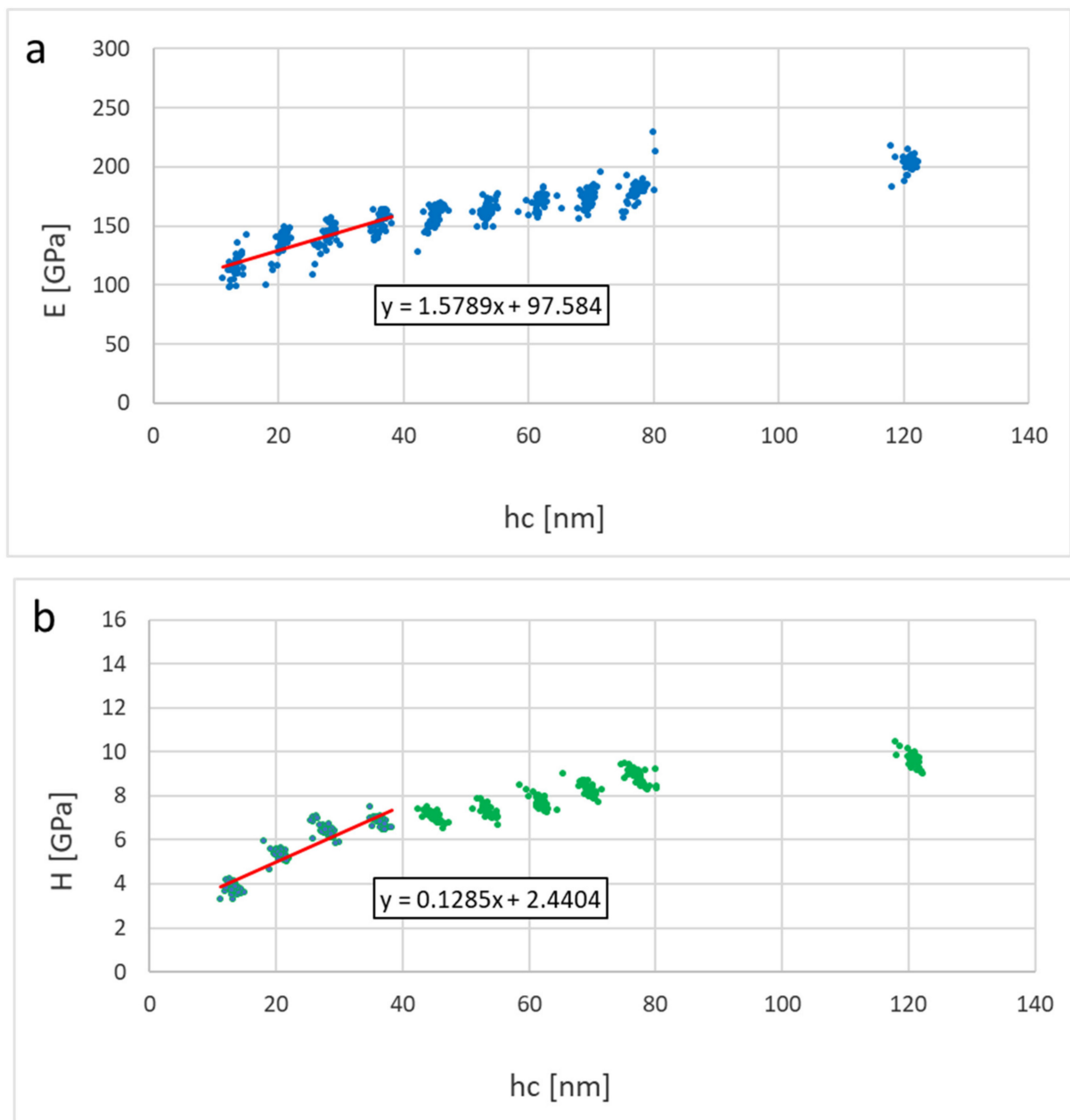


**Figure 10.** Results for  $Ti_2SnC_{Ar^+}TNCF$  (a) Young's modulus vs. contact depth, (b) hardness vs. contact depth.

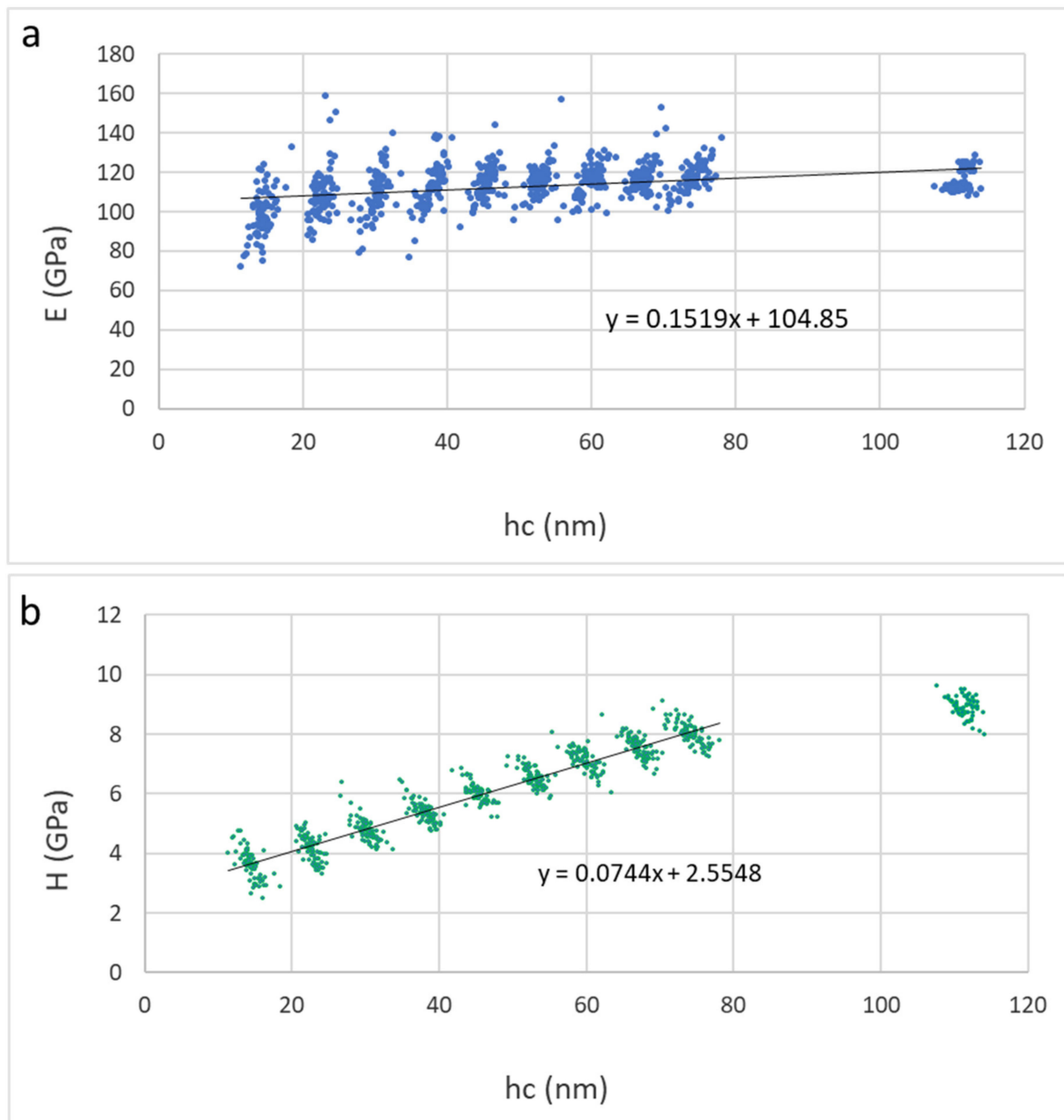


**Figure 11.** Results for  $Ti_2SnC\_PPS$  pristine (a) Young's modulus vs. contact depth, (b) hardness vs. contact depth.

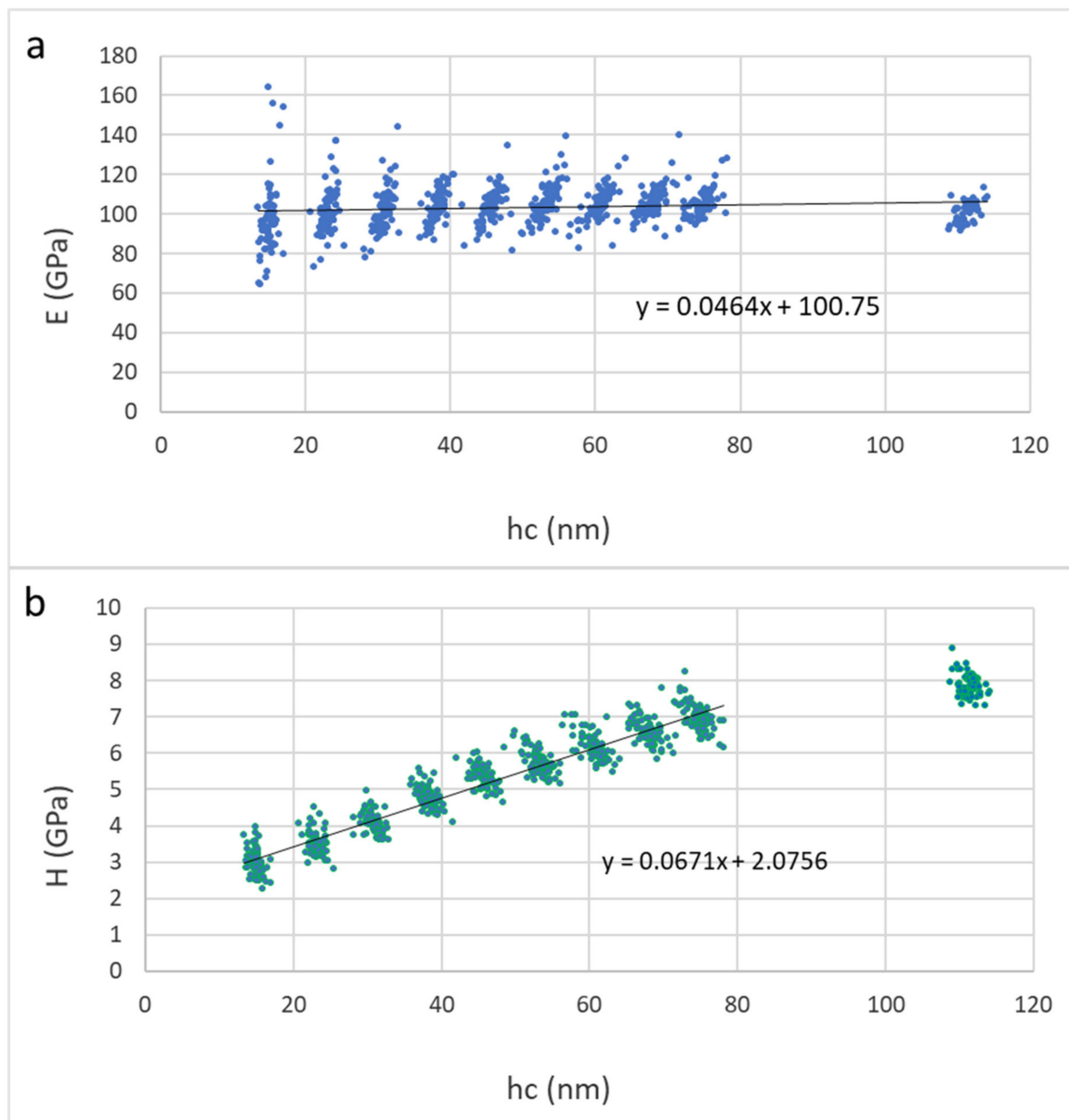


**Figure 12.** Results for  $Ti_2SnC\_PPS$  irradiated (a) Young's modulus vs. contact depth, (b) hardness vs. contact depth.

The data for the irradiated  $Ti_2SnC\_Ar^+TNCf$  shows commensurable hardness with  $Ti_2SnC\_AGTNCf$ , which means that even irradiated with an  $Ar^+$  ion beam, this material may have a high resistance to plastic straining. It seems logical to predict the role of Sn in affecting the mechanical properties of the irradiated film. It was recently reported [58] that a negligible amount of 0.1 at.% of Sn in binary Al/Cu alloys could enhance the hardening of the resultant Al/Cu/Sn material even in low temperatures (100–200 °C). Our EDS analysis finds out ~20 at.%  $\beta$ -Sn in  $Ti_2SnC\_Ar^+TNCf$ . Therefore, our results are in line with the statement that the concentration of Sn is the most liable concerning the hardness properties of the materials. On the other hand, more significant elastic modulus increases than those for the  $Ti_2SnC\_AGTNCf$  were observed. Based on the HAADF-STEM results, we could assume that the microsegregation of Sn atoms on the  $Ti_{0.98}C$  surface could involve local shear strain [59,60]. Local modulation of the  $Ti_2SnC\_Ar^+TNCf$  structure with point defects/voids (marked with red arrows in Figure S5a–d) is well established [61]. Probably due to a low degree of surface defects and low concentration of microsegregation conducted by Sn, the elas-



tic modulus of the  $\text{Ti}_2\text{SnC\_Ar}^+\text{TNCF}$  is not seriously affected. The nanoindentation results for  $\text{Ti}_2\text{SnC\_AGTNCF}$  and  $\text{Ti}_2\text{SnC\_Ar}^+\text{TNCFs}$  are graphically presented in Figures 9 and 10. The hardness value and Young's modulus for  $\text{Ti}_2\text{SnC\_PPB}$  are higher when compared to those obtained for  $\text{Ti}_2\text{SnC\_AGTNCF}$  and  $\text{Ti}_2\text{SnC\_Ar}^+\text{TNCFs}$  (Table 1). Additionally, Young's modulus for  $\text{Ti}_2\text{SnC\_PPB}$  irradiated is higher than those of  $\text{Ti}_2\text{SnC\_AGTNCF}$  and  $\text{Ti}_2\text{SnC\_Ar}^+\text{TNCFs}$ . The Young's modulus and hardness for  $\text{Ti}_2\text{SnC\_PPB}$  (pristine) and  $\text{Ti}_2\text{SnC\_PPB}$  irradiated are graphically presented in Figures 11 and 12, respectively. Although it is hard to generalize, the reason for such a difference between mechanical properties of bulk and thin films may be a dependency on material properties. For instance: (i) the  $\text{Ti}_2\text{SnC\_AGTNCF}$  and  $\text{Ti}_2\text{SnC\_Ar}^+\text{TNCF}$  are thin enough, which can lead to their higher defect density when correlated with bulk  $\text{Ti}_2\text{SnC}$  PPS, (ii) preferred orientation of grains in a sputter-deposited *c*-axis oriented  $\text{Ti}_2\text{SnC}$  films. We can assume that irradiation could maximize the coupling between grains that can reflect the degree of texture and mechanical properties as well [62,63], (iii) differences in grain size between  $\text{Ti}_2\text{SnC\_AGTNCF}$  (~13–14 nm) and  $\text{Ti}_2\text{SnC\_Ar}^+\text{TNCF}$  (~15–16 nm), and  $\text{Ti}_2\text{SnC\_PPB}$  (grains size  $\geq 100$  nm) (see the size distribution for  $\text{Ti}_2\text{SnC\_AG}$  and  $\text{Ti}_2\text{SnC\_Ar}^+\text{TNCF}$  in Figure S6 obtained by ImageJ software (Madison, WI, USA)) [64], and Section 3.6. Surprisingly, the particle size distribution of the irradiated  $\text{Ti}_2\text{SnC\_Ar}^+\text{TNCF}$  was found to follow the same order as before irradiation (see Figure S6), probably due to variation of the phase composition in  $\text{Ti}_2\text{SnC\_Ar}^+\text{TNCF}$ . This result suggested that non-only thin nanocrystalline films with an average size below 20 nm could be considered as effective materials with enhanced radiation damage tolerance, but powdered polycrystalline  $\text{Ti}_2\text{SnC}$  could be considered as a promising resistant material when irradiated with  $\text{Ar}^+$  ion beam, the fluence of which does not go over  $10^{15} \text{ cm}^{-2}$  [65,66].

#### 4. Conclusions

- In conclusion, the microstructure and mechanical properties of  $\text{Ti}_2\text{SnC}$  TNCFs, synthesized by an unconventional low-energy ion facility (LEIF) based on  $\text{Ar}^+$  ion beam sputtering of the Ti, Sn, and C targets have been investigated. Combining high-resolution HAADF-STEM analysis with simulations of SAED patterns, observed that  $\text{Ti}_2\text{SnC\_AGTNCFs}$  coexist with SnO due to oxidation of Sn during the preparation process. A significant microstructural instability was observed after irradiation of the  $\text{Ti}_2\text{SnC\_AGTNCFs}$  with  $\text{Ar}^+$  ion beam having an energy of 30 keV and fluence of  $1.10^{15} \text{ cm}^{-2}$ . The results from simulated SEAD patterns are compatible with experimental HAADF-STEM analysis and have suggested the existence of a heterostructure composed of binary  $\text{Ti}_{0.98}\text{C}$  carbide and metallic  $\beta\text{-Sn}$ , which could be attributed to the irradiation-induced instability of the ultrathin  $\text{Ti}_2\text{SnC}$  film. In addition,  $\text{Ar}^+$  ion-beam irradiation-induced dislocation and point defects can provide channels for very fast Sn mass transport. The analysis by nanoindentation showed that the irradiated  $\text{Ti}_2\text{SnC}$  TNCFs and irradiated  $\text{Ti}_2\text{SnC\_PPS}$  exhibited promising Young's modulus and hardness even for the locally disordered structure in  $\text{Ti}_2\text{SnC}$  TNCFs. This fact opens the possibility of exploiting the  $\beta\text{-Sn}/\text{Ti}_{0.98}\text{C}$  structure as a composite where a harsh radiation environment could have occurred.
- HRTEM/SAED observations and XRD analyses of the  $\text{Ti}_2\text{SnC\_PPS}$  documented 70.4% of a single  $\text{Ti}_2\text{SnC}$  phase. The calculated value for NPs size by Scherrer's formula was estimated to be 120 nm. The presence of 9% of Sn avoided the formation of stable intermetallic impurities ( $\text{Ti}_3\text{Sn}$ ,  $\text{Ti}_6\text{Sn}_5$ ,  $\text{Ti}_2\text{Sn}$ , and  $\text{Ti}_5\text{Sn}_3$ ) in  $\text{Ti}_2\text{SnC\_PPS}$ . The  $\text{Ti}_2\text{SnC\_PPS}$  irradiated yield the lowest hardness (H) when compared with  $\text{Ti}_2\text{SnC\_PPS}$  and unirradiated and irradiated  $\text{Ti}_2\text{SnC}$  TNCFs. Probably, the low degree of nanocrystallinity and tendency to agglomeration upon irradiation can contribute to the surface hardness of polycrystalline bulk materials.
- The approach here presented may be extendable to other  $\text{M}_2\text{AX}$  nanostructured materials, and can keep attention for material science applications ranging from protective

nanocoating films, ion-beam irradiation resistant parts for nuclear applications and nanoceramics, to their utilization as a precursor for MX phases.

**Supplementary Materials:** The following are available online at <https://www.mdpi.com/article/10.3390/nano12030307/s1>, Figure S1: Morphology of Ti<sub>2</sub>SnC M<sub>2</sub>AX samples (a) Ti<sub>2</sub>SnC\_AGTNCF, (b) Ti<sub>2</sub>SnC\_Ar<sup>+</sup>TNCF and (c) Ti<sub>2</sub>SnC\_PPS obtained by SEM with SE detector; Figure S2: (a) EDS-STEM analysis and (b) EDS-STEM mapping Ti<sub>2</sub>SnC\_AGTNCF. HAADF-STEM image of Ti<sub>2</sub>SnC\_AGTNCF at low magnification and Table with at. % of elements are present as an inset in Figure S2a; Figure S3: (a) EDS-STEM analysis and (b) EDS-STEM mapping Ti<sub>2</sub>SnC\_Ar<sup>+</sup>TNCF. HAADF-STEM image of Ti<sub>2</sub>SnC\_Ar<sup>+</sup>TNCF at low magnification and Table with at. % of elements are present as an inset in Figure S3a; Figure S4: XRD pattern of Ti<sub>2</sub>SnC PPS: Titanium Tin Carbide Ti<sub>2</sub>SnC–70.4% Reference code: 04-005-0037, Tin Sn–9.1% Reference code: 04-004-7745, Titanium Carbide TiC0.55–11.2% Reference code: 04-018-5143, Titanium Tin Carbide Ti<sub>2</sub>SnC–9.3% Reference code: 04-005-0049; Figure S5: (a–d) HRTEM images of irradiation-induced defect cores in Ti<sub>2</sub>SnC\_Ar<sup>+</sup>TNCF. The yellow marked regions indicated defect cores in a different region of interest, where the interaction of dislocation lines, voids, and atoms segregated on the surface (marked with red arrows) are well visible; Figure S6. STEM images and corresponding particle size distribution estimated by ImageJ software [64]. (a) Ti<sub>2</sub>SnC\_AGTNCF and (b) Ti<sub>2</sub>SnC\_Ar<sup>+</sup>TNCF.

**Author Contributions:** Conceptualization, S.B. and J.V.; methodology, J.P.; software, G.C. and B.I.; validation, B.I., V.L. and J.K.; formal analysis, G.C.; investigation, J.N.; resources, S.B.; data curation, J.N.; writing—original draft preparation, J.V. and B.I.; writing—review and editing, S.B.; visualization, G.C.; supervision, S.B., Š.M. and R.K.; project administration, J.V.; funding acquisition, S.B. and J.V. All authors have read and agreed to the published version of the manuscript.

**Funding:** This research is funded by the Czech Science Foundation (project No. 18-21677S). This work was supported by OP VVV Project Development of new nano and micro coatings on the surface of selected metallic materials–NANOTECH ITI II. Reg. No. CZ.02.1.01/0.0/0.0/18\_069/0010045. The aberration-corrected JEOL ARM200CF at UIC Chicago was acquired using two grants from the National Science Foundation (DMR-0959470, DMR-1626065).

**Institutional Review Board Statement:** Not applicable.

**Informed Consent Statement:** Informed consent was obtained from all subjects involved in the study.

**Data Availability Statement:** MDPI Research Data Policies at <https://www.mdpi.com/ethics> (accessed on 12 January 2022).

**Acknowledgments:** We would like to thank the reviewers for their thoughtful comments and efforts towards improving our manuscript.

**Conflicts of Interest:** The authors declare no conflict of interest.

## References

1. Barsoum, M.W. The M<sub>n+1</sub>AX<sub>n</sub> Phases: A new class of solids: Thermodynamically stable nanolaminates. *Prog. Solid State Chem.* **2000**, *28*, 201–281. [[CrossRef](#)]
2. Eklund, P.; Beckers, M.; Jansson, U.; Hogberg, H.; Hultman, L. The M<sub>n+1</sub>AX<sub>n</sub> Phases: Materials science and thin-film processing. *Thin. Solid Film.* **2010**, *518*, 1851–1878. [[CrossRef](#)]
3. Jeitschko, W.; Nowotny, H.; Benesovsky, F. Kohlenstoffhaltige ternäre verbindungen (H-phase). *Mon. Chem. Verwandte Teile And. Wiss.* **1963**, *94*, 672–676. [[CrossRef](#)]
4. Barsoum, M.W.; El-Raghy, T. The Max Phases: Unique new carbide and nitride materials: Ternary ceramics turn out to be surprisingly soft and machinable, yet also heat-tolerant, strong and lightweight. *Am. Sci.* **2001**, *89*, 334–343. [[CrossRef](#)]
5. Tallman, D.J. On the Potential of Max Phases for Nuclear Applications. Ph.D. Thesis, Drexel University, Philadelphia, PA, USA, June 2015.
6. Whittle, K.R.; Blackford, M.G.; Aughterson, R.D.; Moricca, S.; Lumpkin, G.R.; Riley, D.P.; Zaluzec, N.J. Radiation tolerance of M<sub>n+1</sub>AX<sub>n</sub> Phases, Ti<sub>3</sub>AlC<sub>2</sub> and Ti<sub>3</sub>SiC<sub>2</sub>. *Acta Mater.* **2010**, *58*, 4362–4368. [[CrossRef](#)]
7. Liu, C.; Shi, L.; Qi, Q.; O'Connor, D.J.; King, B.V.; Kisi, E.H.; Qing, X.B.; Wang, B.Y. Surface damage of Ti<sub>3</sub>SiC<sub>2</sub> By Mev Iodine bombardment. *Nucl. Instrum. Methods Phys. Res. Sect. B: Beam Interact. Mater. At.* **2013**, *307*, 536–540. [[CrossRef](#)]
8. Wu, J.Y.; Zhou, Y.C.; Wang, J.Y. Tribological behavior of Ti<sub>2</sub>SnC particulate reinforced copper matrix composites. *Mater. Sci. Eng.* **2006**, *422*, 266–271. [[CrossRef](#)]

9. Dong, H.Y.; Yan, C.K.; Chen, S.Q.; Zhou, Y.C. Solid–Liquid reaction synthesis and thermal stability of Ti<sub>2</sub>SnC powders. *J. Mater. Chem.* **2001**, *11*, 1402–1407. [[CrossRef](#)]
10. Li, Y.; Bai, P. The microstructural evolution of Ti<sub>2</sub>SnC from Sn–Ti–C system by Self-propagating High-temperature Synthesis (SHS). *Int. J. Refract. Met. Hard Mater.* **2011**, *29*, 751–754. [[CrossRef](#)]
11. Li, S.; Bei, G.-P.; Zhai, H.-X.; Zhou, Y. Bimodal microstructure and reaction mechanism of Ti<sub>2</sub>SnC synthesized by a high-temperature reaction using Ti/Sn/C and Ti/Sn/TiC powder compacts. *J. Am. Ceram. Soc.* **2006**, *89*, 3617–3623. [[CrossRef](#)]
12. Yeh, C.L.; Kuo, C.W. Effects of TiC addition on formation of Ti<sub>2</sub>SnC by self-propagating combustion of Ti–Sn–C–TiC powder compacts. *J. Alloy. Compd.* **2010**, *502*, 461–465. [[CrossRef](#)]
13. Li, S.; Bei, G.-P.; Zhai, H.-X.; Zhou, Y. Synthesis of Ti<sub>2</sub>SnC from Ti/Sn/TiC powder mixtures by pressureless sintering technique. *Mater. Lett.* **2006**, *60*, 3530–3532. [[CrossRef](#)]
14. Guillon, O.; Gonzales-Julian, J.; Dargatz, B.; Kessel, T.; Schierning, G.; Rathel, J.; Herrmann, M. Field-assisted sintering technology/spark plasma sintering: Mechanisms, materials, and technology developments. *Adv. Eng. Mater.* **2014**, *16*, 830–849. [[CrossRef](#)]
15. Lu, C.; Wang, Y.; Wang, X.; Zhang, J. Synthesis of Ti<sub>2</sub>SnC under optimized experimental parameters of pressureless spark plasma sintering assisted by Al addition. *Adv. Mater. Sci. Eng.* **2018**, *2018*, 9861894. [[CrossRef](#)]
16. Canam Project. Available online: <http://www.Ujf.Cas.Cz/En/Research-Development/Large-Research-Infrastructures-And-Centres/Canam/About-The-Project/> (accessed on 12 December 2021).
17. Bakardjieva, S.; Ceccio, G.; Vacik, J.; Calcagno, L.; Cannavo, A.; Horak, P.; Lavrentiev, V.; Nemecek, J.; Michalcova, A.; Klie, R. Surface morphology and mechanical properties changes induced in Ti<sub>3</sub>InC<sub>2</sub> (M<sub>3</sub>AX<sub>2</sub>) thin nanocrystalline films by irradiation of 100 KeV Ne<sup>+</sup> ions. *Surf. Coat. Technol.* **2021**, *426*, 127775. [[CrossRef](#)]
18. Gates-Rector, S.D.; Blanton, T.N. The Powder Diffraction File: A Quality Materials Characterization Database. *Powder Diffr.* **2019**, *34*, 352–360. [[CrossRef](#)]
19. Lábár, J.L. Consistent Index. A (Set) SAED Pattern(S) ProcessDiffraction Program. *Ultramicroscopy* **2005**, *103*, 237–249.
20. Klie, R.F.; Zheng, J.C.; Zhu, Y.; Varela, M.; Wu, J.; Leighton, C. Direct measurement of the low-temperature spin-state transition in LaCoO<sub>3</sub>. *Phys. Rev. Lett.* **2007**, *99*, 047203. [[CrossRef](#)]
21. Zhang, J.; Liu, B.; Wang, J.Y.; Zhou, Y.C. Low-temperature instability of Ti<sub>2</sub>SnC: A combined transmission electron microscopy, differential scanning calorimetry, and X-ray diffraction investigations. *J. Mater. Res.* **2009**, *24*, 39–49. [[CrossRef](#)]
22. Cannavò, A.; Vacik, J.; Bakardjieva, S.; Kupcik, J.; Lavrentiev, V.; Ceccio, G.; Horak, P.; Nemecek, J.; Calcagno, L. Effect of medium energy He<sup>+</sup>, Ne<sup>+</sup> And Ar<sup>+</sup> ion irradiation on the Hf–In–C thin film composites. *Thin. Solid Films* **2021**, *743*, 139025. [[CrossRef](#)]
23. Dias, J.S.; Batista, F.R.M.; Bacani, R.; Triboni, E.R. Structural characterization of SnO nanoparticles synthesized by the hydrothermal and microwave routes. *Sci. Rep.* **2020**, *10*, 9446. [[CrossRef](#)]
24. Vázquez-López, A.; Maestre, D.; Ramirez-Castellanos, J.; Cremades, A. In situ local oxidation of SnO induced by laser irradiation: A stability study. *Nanomaterials* **2021**, *11*, 976. [[CrossRef](#)]
25. Jaśkaniec, S.; Kavanagh, S.R.; Coelho, J.; Ryan, S.; Hobbs, C.; Walsh, A.; Scanlon, D.O.; Nicolosi, V. Solvent engineered synthesis of layered SnO for high-performance anodes. *npj 2D Mater. Appl.* **2021**, *5*, 27. [[CrossRef](#)]
26. Campo, C.M.; Rodríguez, J.E.; Ramírez, A.E. Thermal behaviour of romarchite phase SnO in different atmospheres: A hypothesis about the phase transformation. *Heliyon* **2016**, *2*, E00112. [[CrossRef](#)] [[PubMed](#)]
27. Moreno, M.S.; Egerton, R.F.; Midgley, P.A. Differentiation of Tin Oxides using electron energy-loss spectroscopy. *Phys. Rev. B* **2004**, *69*, 233304. [[CrossRef](#)]
28. Adelman, C.; Brault, J.; Rouviere, J.-R.; Mariette, H.; Mula, G.; Daudin, B. Atomic-layer epitaxy of GaN quantum wells and quantum dots on (0001) AlN. *J. Appl. Phys.* **2002**, *91*, 5498–5500. [[CrossRef](#)]
29. Voyles, P.M.; Muller, D.A.; Grazul, J.L.; Citrin, P.H.; Gossmann, H.J. Atomic-scale imaging of individual dopant atoms and clusters in highly N-Type bulk Si. *Nature* **2002**, *416*, 826–829. [[CrossRef](#)]
30. Rafferty, B.; Nellist, D.; Pennycook, J. On the origin of transverse incoherence in z-contrast stem. *Microscopy* **2001**, *50*, 227–233. [[CrossRef](#)]
31. Williams, R.K.; Wiffen, F.W.; Bentley, J.; Stiegler, J.O. Irradiation induced precipitation in tungsten based, W–Re alloys. *Metall. Trans.* **1983**, *14*, 655–666. [[CrossRef](#)]
32. Nordlund, K.; Averback, R.S. Point defect movement and annealing in collision cascades. *Phys. Rev.* **1997**, *56*, 2421. [[CrossRef](#)]
33. Haberland, H. A model for the processes happening in a rare-gas cluster after ionization. *Surf. Sci.* **1985**, *156*, 305–312. [[CrossRef](#)]
34. Ding, A.; Futrell, J.H.; Cassidy, R.A.; Cordis, L.; Hesslich, J. Mass spectrometric and photoionisation investigations of the structure of heterogeneous clusters. *Surf. Sci.* **1985**, *156*, 282–291. [[CrossRef](#)]
35. Begemann, W.; Dreihöfer, S.; Meiwes-Broer, K.H.; Lutz, H.O. Sputtered metal cluster ions: Unimolecular decomposition and collision induced fragmentation. *Z. Phys. D At. Mol. Clust.* **1986**, *3*, 183–188. [[CrossRef](#)]
36. Fondell, M.; Gorgoi, M.; Boman, M.; Lindblad, A. An HAXPES study of Sn, SnS, SnO and SnO<sub>2</sub>. *J. Electron. Spectrosc. Relat. Phenom.* **2014**, *195*, 195–199. [[CrossRef](#)]
37. Hayashi, Y.; Matsumoto, K. Fragmentation of Sputtered Neutrals by SNMS. *J. Mass Spectrom. Soc. Jpn.* **1991**, *39*, 93–96. [[CrossRef](#)]
38. Chapon, C.; Gillet, M.F.; Henry, C.R. (Eds.) *Small Particles and Inorganic Clusters: Proceedings of the Fourth International Meeting on Small Particles and Inorganic Clusters University Aix-Marseille III Aix-en-Provence*; Springer Science & Business Media: Marseille, France, 2012.

39. Bras, P.; Sterner, J.; Platzer-Björkman, C. Investigation of blister formation in sputtered  $\text{Cu}_2\text{ZnSnS}_4$  absorbers for thin film solar cells. *J. Vac. Sci. Technol. A: Vac. Surf. Film.* **2015**, *33*, 061201. [[CrossRef](#)]
40. Hardy, H.K.; Silcock, J.M. The Phase Sections at 500 and 350 °C of Al Rich Al-Cu-Li Alloys. *J. Inst. Met.* **1955**, *84*, 423–428.
41. Parish, C.M.; Field, K.G.; Certain, A.G.; Wharry, J.P. Application of STEM Characterization for Investigating Radiation Effects in BCC Fe-Based. *J. Mater. Res.* **2015**, *30*, 1275–1289. [[CrossRef](#)]
42. Schäublin, R. Effect of helium on irradiation-induced hardening of iron: A simulation point of view. *J. Nucl. Mater.* **2007**, *362*, 152–160. [[CrossRef](#)]
43. Riviere, J.P. Radiation Induced Point Defects and Diffusion. In *Application of Particle and Laser Beams in Materials Technology*; Misaelides, P., Ed.; NATO ASI Series (Applied Sciences); Springer: Dordrecht, The Netherlands, 1995; Volume 283. [[CrossRef](#)]
44. Lecterc, S.J.; Li, X.; Lescoat, M.L.; Fortuna, F.; Gentils, A. Microstructure of Au-ion irradiated 316L and FeNiCr austenitic stainless steels. *J. Nucl. Mater.* **2016**, *480*, 436–446.
45. Lapauw, T.; Tunca, B.; Potashnikov, D.; Pesach, A.; Ozeri, O.; Vleugels, J.; Lambrinou, K. The double solid solution  $(\text{Zr, Nb})_2(\text{Al, Sn})\text{C}$  MAX phase: A steric stability approach. *Sci. Rep.* **2018**, *8*, 12801. [[CrossRef](#)] [[PubMed](#)]
46. Titus, M.S.; Rhein, R.K.; Wells, P.B.; Dodge, P.C.; Viswanathan, G.B.; Mills, M.J.; Van derVan, A.; Pollock, T.M. Solute segregation and deviation from bulk thermodynamics at nanoscale crystalline defects. *Sci. Adv.* **2016**, *2*, e1601796. [[CrossRef](#)]
47. Mukherjee, S.; Assali, S.; Oussama Moutanabbir, O. Atomic Pathways of Solute Segregation in the Vicinity of Nanoscale Defects. *Nano Lett.* **2021**, *23*, 9882–9888. [[CrossRef](#)] [[PubMed](#)]
48. Rathika, R.; Kovendhan, M.; Paul Joseph, D.; Vijayarangamuthu, K.; Sendil Kamur, A.; Venkateswaran, C.; Asokan, K.; Johnson Jeyakumar, S. 200 MeV  $\text{Ag}^{15+}$  ion beam irradiation induced modifications in spray deposited  $\text{MoO}_3$  thin films by fluence variation. *Nucl. Eng. Technol.* **2019**, *51*, 1983–1990. [[CrossRef](#)]
49. Wang, J.Y.; Zhou, Y.C.; Liao, T.; Zhang, J.; Lin, Z.J. A first principles investigation of the phase stability of  $\text{Ti}_2\text{AlC}$  with Al vacancies. *Scr. Mater.* **2008**, *58*, 227–231. [[CrossRef](#)]
50. Herring, C.; Galt, J.K. Elastic and plastic properties of very small metal specimens. *Phys. Rev.* **1952**, *85*, 1060. [[CrossRef](#)]
51. Sears, G.W. A mechanism of whisker growth. *Acta Metall.* **1955**, *3*, 367. [[CrossRef](#)]
52. Tu, K.N.; Thompson, R.D. Kinetics of interfacial reaction in bimetallic Cu-Sn thin films. *Acta Metall.* **1982**, *30*, 947–952. [[CrossRef](#)]
53. Zenou, V.Y.; Bakardjieva, S. Microstructural analysis of undoped and moderately Sc-doped  $\text{TiO}_2$  anatase nanoparticles using Scherrer equation and Debye function analysis. *Mater. Charact.* **2018**, *144*, 287–296. [[CrossRef](#)]
54. Barsoum, M.W.; Yaroschuk, G.; Tyagi, S. Fabrication and characterization of  $\text{M}_2\text{SnC}$  (M= Ti, Zr, Hf and Nb). *Scr. Mater.* **1997**, *37*, 1583–1591. [[CrossRef](#)]
55. Yin, F.; Tedenac, J.C.; Gascoin, F. Thermodynamic modelling of the Ti-Sn system and calculation of the Co-Ti-Sn system. *Comput. Coupling Phase Diagr. Thermochem.* **2007**, *31*, 370–379. [[CrossRef](#)]
56. Yang, J.Y.; Kim, W.J. The effect of addition of Sn to copper on hot compressive deformation mechanisms, microstructural evolution and processing maps. *J. Mater. Res. Technol.* **2020**, *9*, 749–761. [[CrossRef](#)]
57. Oliver, W.C.; Pharr, G.M. An improved technique for determining hardness and elastic modulus using load and displacement sensing indentation experiments. *J. Mater. Res.* **1992**, *7*, 1564–1583. [[CrossRef](#)]
58. Lapauw, T.; Vanmeensel, K.; Lambrinou, K.; Vleugels, J. Rapid synthesis and elastic properties of fine-grained  $\text{Ti}_2\text{SnC}$  produced by spark plasma sintering. *J. Alloy. Compd.* **2015**, *631*, 72–76. [[CrossRef](#)]
59. Nie, J.F. Applications of atomic-resolution HAADF-STEM and EDS-STEM characterization of light alloys. In *IOP Conference Series: Materials Science and Engineering*; IOP Publishing: Riso, Denmark, 2017; p. 012005. [[CrossRef](#)]
60. Nie, J.F.; Aaronson, H.I.; Muddle, B.C. *Proceedings of an International Conference on Solid-Solid Phase Transform*; Koiwa, M., Otsuka, K., Miyazaki, T., Eds.; The Japan Institute of Metals: Tokyo, Japan, 1999; p. 157.
61. Nie, J.F.; Muddle, B.C. The lattice correspondence and diffusional-displacive phase transformations. *Mater. Forum* **1999**, *23*, 23–40.
62. Bakardjieva, S.; Horak, P.; Vacik, J.; Cannavo, A.; Lavrentiev, V.; Torrisi, A.; Michalcova, A.; Klie, R.; Rui, X.; Calcagno, L. Effect of  $\text{Ar}^+$  irradiation of  $\text{Ti}_3\text{InC}_2$  at different ion beam fluences. *Surf. Coat. Technol.* **2020**, *394*, 125834. [[CrossRef](#)]
63. Högberg, H.; Emmerlich, J.; Eklund, P.; Wilhelmsson, O.; Palmquist, J.P.; Jansson, U.; Hultman, L. Growth and property characterization of epitaxial MAX-phase thin films from the  $\text{Ti}_{n+1}(\text{Si, Ge, Sn})\text{C}_n$  systems. In *Advances in Science and Technology*; Trans Tech Publications Ltd.: Acireale, Italy, 2006; Volume 45, pp. 2648–2655.
64. Rueden, C.T.; Schindelin, J.; Hiner, M.C.; DeZonia, B.E.; Walter, A.E.; Arena, E.T.; Eliceiri, K.W. ImageJ2: ImageJ for the next generation of scientific image data. *BMC Bioinform.* **2017**, *18*, 529. [[CrossRef](#)] [[PubMed](#)]
65. Kalita, P.; Ghosh, S.; Gutierrez, G.; Rajput, P.; Grover, V.; Sattonnay, G.; Avasthi, D.K. Grain size effect on the radiation damage tolerance of cubic zirconia against simultaneous low and high energy heavy ions: Nano triumphs bulk. *Sci Rep.* **2021**, *11*, 10886. [[CrossRef](#)]
66. Liew, P.J.; Yap, C.Y.; Wang, J. Surface modification and functionalization by electrical discharge coating: A comprehensive review. *Int. J. Extrem. Manuf.* **2020**, *2*, 012004. [[CrossRef](#)]